

CO IN THE DISK OF THE BARRED SPIRAL GALAXY M83: CO (1–0), CO (2–1), AND NEUTRAL GAS

LUCIAN P. CROSTHWAITE, JEAN L. TURNER, AND LEAH BUCHHOLZ

Division of Astronomy and Astrophysics, Department of Physics and Astronomy, UCLA, Los Angeles, CA 90095;
lucian@astro.ucla.edu, turner@astro.ucla.edu, leahmartin@juno.com

PAUL T. P. HO

Harvard-Smithsonian Center for Astrophysics, 60 Garden Street, Cambridge, MA 02138; pho@cfa.harvard.edu

AND

ROBERT N. MARTIN

Institute of Astronomy and Astrophysics, Academia Sinica, 128, Section 2, P.O. Box 1-87, Nankang, 115 Taipei, Taiwan;
rmartin@cfa.harvard.edu, robert@asiaa.sinica.edu.tw

Received 2001 April 6; accepted 2002 January 2

ABSTRACT

We present “on-the-fly” maps of CO (1–0) and CO (2–1) in the barred spiral galaxy M83. The entire optical disk is filled with CO emission in both lines, including interarm regions. For a “standard” conversion factor the total molecular mass is $2.5 \times 10^9 M_{\odot}$, 4% of the total dynamical mass. Molecular gas constitutes 80% of total gas mass within the inner $10'$ and 30% overall. CO (1–0) emission and 21 cm continuum emission are extremely well correlated spatially in regions where H_2 dominates the gas surface density. The spatial correlation between CO (1–0) and $100 \mu\text{m}$ emission is not as good. While the kinematics of the outer H I disk is severely nonaxisymmetrically perturbed, the kinematics of the CO disk and inner H I disk is well behaved and circular. The molecular disk appears to have a distinct hard edge at $5'$. The hard edge is accompanied by a steep decline in the total gas surface density at that radius, although the H I does continue outward at a lower level. This edge is coincident with the onset of strong warping of the outer disk. The mean ratio of CO (2–1)/CO (1–0) emission is ~ 1 , high by Galactic standards. Peaks in this ratio in interarm regions suggest that the CO emission is optically thin there, among other possibilities. Thus, M83 is unusual in that it has a relatively axisymmetric, almost entirely molecular, inner $10'$ gas disk surrounded by a warped, entirely atomic, outer gas disk. A sharp discontinuity separates the inner and outer gas disks. This kind of gas distribution is not seen in other late-type, gas-rich spirals.

Key words: galaxies: individual (M83, NGC 5236) — galaxies: ISM — galaxies: spiral — galaxies: structure — ISM: molecules

1. INTRODUCTION

Study of molecular gas in galaxies is difficult since one cannot detect cold H_2 directly. Instead, the brightest molecular lines of CO are used as a proxy. CO emission is weak in other galaxies, and few fully sampled images of CO emission in galaxies exist. Early studies established that CO emission is strongest in the central regions of spiral galaxies (Young & Scoville 1991 and references therein); that it falls off, as does blue light, in a near exponential manner with galactocentric distance (Young & Scoville 1982); that it is present in early- as well as late-type spirals (Young et al. 1995); and that it is less abundant in dwarf or low-metallicity galaxies (Sage et al. 1992). Similar behavior is inferred for H_2 . While the general radial dependence is well studied, the lack of fully sampled images means that the axisymmetric distribution of H_2 is poorly known, as is its relation to the atomic component.

As part of a program of deep mapping of CO in nearby galaxies, we have observed the nearby galaxy M83 (4 Mpc; de Vaucouleurs 1979). M83 is a nearly face-on, gas-rich Sbc spiral galaxy with a starburst nucleus (Rieke 1976; Bohlin et al. 1983; Trinchieri, Fabiano, & Paulumbo 1985; Turner, Ho, & Beck 1987; Tellesco, Wolstencroft, & Done 1988; Turner & Ho 1994). It has a pronounced bar and thick spiral arms with well-defined dust lanes and vigorous star formation (Rumstay & Kaufman 1983; Handa et al. 1990; Wiklind et al. 1990; Lord & Kenney 1991; Kenney & Lord 1991; Tilanus &

Allen 1993; Deutsch & Allen 1993; Rand, Lord, & Higdon 1999). The atomic hydrogen (H I) gas disk of M83 is over 1° in diameter (Huchtmeier & Bohnenstengel 1981). The H I velocity field indicates a severe warping of the outer gas disk, possibly due to an interaction with the dwarf galaxy NGC 5253 (Rogstad, Lockhart, & Wright 1974) located at a projected distance of 200 kpc. The central $10'$ of the H I disk shows spiral arms coincident with the optical pattern and a central depression within the inner $2'$ (Tilanus & Allen 1993).

Numerous studies have covered specific aspects of the CO in M83: arm and interarm molecular clouds in the southeastern portion of the optical disk (Wiklind et al. 1990); molecular gas in the eastern arm (Lord & Kenney 1991; Rand et al. 1999); molecular gas at the bar–spiral arm transition (Kenney & Lord 1991); the bar and nucleus (Handa et al. 1990); the nucleus (Combes et al. 1978; Petitpas & Wilson 1998). However, M83 has never been fully mapped in CO, perhaps because of its southerly location. While a piecewise picture of CO in M83 has emerged, the overall CO morphology of M83 is not well known.

We present maps of CO (1–0) and CO (2–1) covering the $14' \times 14'$ optical disk of M83. We have taken advantage of the “on-the-fly” (OTF) observing mode at the NRAO¹

¹ The National Radio Astronomy Observatory is a facility of the National Science Foundation operated under cooperative agreement by Associated Universities, Inc.

12 m telescope, where the telescope smoothly and repeatedly scans a large field. This mode is well suited to the imaging of extended cold, CO gas. The maps are deep enough to detect cold, extended interarm CO (1–0) to levels of $I_{\text{CO}} \sim 1 \text{ K km s}^{-1}$ and $N_{\text{H}_2} \sim 2 \times 10^{20} \text{ cm}^{-2}$. Observations of CO (2–1) allow us to study the excitation of the gas. We combine these maps with archival data in order to study the total neutral gas distribution across the disk and its relation to the stellar disk.

2. OBSERVATIONS AND DATA REDUCTION

2.1. 12 m CO Observations

Observations of CO (1–0) at 115 GHz and CO (2–1) at 230 GHz were made at the former NRAO 12 m telescope at Kitt Peak, on separate observing runs between 1995 February and 1998 March. An equivalent of ~ 40 hr of on-source observing was accumulated for each CO line. Calibration was done by the chopper wheel method (Ulich & Hass 1976). We convert the recorded T_r^* values (Kutner & Ulich 1981) to main-beam temperature, $T_{\text{mb}} = T_r^* / \eta_m^*$, using corrected main-beam efficiency, $\eta_m^* = 0.88 \pm 0.04$ at 115 GHz and $\eta_m^* = 0.56 \pm 0.06$ at 230 GHz (Mangum 1996b, 1997).² We report $T_{\text{CO}} = T_{\text{mb}}$ throughout this paper. The filterbank spectrometer was configured for 2 MHz channel widths with 256 total channels, producing spectral channels of a 5.2 km s^{-1} width at 115 GHz and 2.6 km s^{-1} at 230 GHz. The total bandwidth of 512 MHz was tuned to a systemic velocity (LSR) of 510 km s^{-1} .

The OTF observing mode was used (Mangum 1996a).³ Scanning rates between $30''$ and $40'' \text{ s}^{-1}$ and scan row spacings of $18''$ at 115 GHz and $8''$ at 230 GHz were selected to ensure better than Nyquist sampling over the $18' \times 18'$ region. The beam size (FWHM) of the 12 m telescope is $55''$ at 115 GHz and $27''.5$ at 230 GHz. Chopper wheel calibration and sky-offs were made every two rows. The initial 16 individual 115 GHz OTF maps covered a $10' \times 10'$ region centered on the nucleus. The initial map was supplemented by 10 OTF maps of strips extending the mapped region out another $4'$ along each side. The strips were mosaicked along with the interior map to form the final $18' \times 18'$ and combined with an additional 11 OTF maps made of the larger region to form the 115 GHz maps presented here. The rms noise level was reduced by averaging the individual OTF maps made at 115 GHz. The 230 GHz OTF maps were all made at the larger mapped region size, and 15 were averaged to reduce the rms noise level.

The OTF data were reduced using the NRAO AIPS package. A linear spectral baseline was removed in each spectrum. A linear baseline was removed from each row of the channel maps (assuming that there is no CO emission present in the first and last few pixels of a scanned row) to reduce the “striping” effect in the scan direction due to sky brightness fluctuations between successive off positions, typically 1 minute apart. Sky brightness fluctuations on timescales shorter than the chopper wheel calibration are not calibrated and are thus present in point-by-point, single-dish maps. However, OTF data, which contain images of sky regions, allow us to estimate the scale of these fluctua-

tions and partially correct for them. To quantify the magnitude of the sky brightness variations, we measured the rms variation in the channel maps before and after “destriping.” Destriping improved the rms noise by 7 mK at 115 GHz and 22 mK at 230 GHz. Destriping may also remove some extended low-level emission, but this consequence is unavoidable with the present data. The mean rms noise from fully reduced, line-free channels is $T_{\text{mb}} = 46$ and 172 mK for CO (1–0) and CO (2–1), respectively. Sky brightness fluctuations appear to be $\sim 10\%$ – 15% of the rms noise value. The CO (2–1) channels were averaged to a 5.2 km s^{-1} channel width to improve the signal-to-noise ratio. The mean rms noise in the averaged channels is $T_{\text{mb}} = 133$ mK. The estimated uncertainty due to uncertainties in the corrected main-beam efficiency and sky brightness fluctuations gives an overall uncertainty of $\sim 15\%$ in T_{mb} .

While the main-beam efficiency at 115 GHz is high enough to allow us to neglect the contribution from the error beam, it is not obvious that the same can be said for the CO (2–1) data. At 230 GHz, $\eta_m^* \sim 0.56$ and the peak amplitude of the error beam is 0.3% of the main-beam peak amplitude. Because the FWHM ~ 8.5 of the error beam is comparable in extent to the CO (2–1) emission, there is a possibility of a significant contribution to the main-beam temperatures from the error beam. We created a model of several frames of the CO (2–1) emission “butterfly” pattern, a model main-beam plus error-beam pattern, and convolved the two patterns. We found that the error beam can contribute 0.1%–0.5% of the peak channel emission, 12 mK, less than 10% of the rms noise in a CO (2–1) channel. The contribution of the error beam is small because of the spatial localization of signal in each spectral channel. The same could not be said if this were a continuum map. We can therefore safely ignore the contribution of the 230 GHz error beam.

All of the detected CO emission was contained within a $12'$ diameter. While larger $18' \times 18'$ regions were mapped, the channel maps presented here were reduced in size to focus on the detected emission.

The quality of the moment maps (integrated intensity and intensity-weighted mean velocity) was improved by using a mask to identify regions of noise within individual channel maps before the sum. We convolved the cube to twice the nominal beam size and used emission greater than 2σ in the convolved cube to construct a mask to clip out regions of noise in the unconvolved cube. This removes isolated, single-pixel noise spikes (less than 3σ) in the unconvolved cube that might dilute the signal in the integrated intensity and velocity maps. Peak intensity (T_{CO}) and integrated intensity (I_{CO}) maps were made from CO emission above 1σ in the masked, clipped, channel cubes. A 1.2σ cut was used for mean velocity and velocity dispersion maps.

The objective of these OTF observations was to map the extent and structure of the H_2 gas in M83. To do so we convert from I_{CO} to N_{H_2} . We use the “standard conversion factor,” X_{CO} (Scoville & Sanders 1987; Young & Scoville 1991). This X_{CO} is estimated to be accurate to a factor of 2 in the Milky Way disk (Solomon et al. 1987 and references therein). X_{CO} appears to underpredict N_{H_2} in low-metallicity galaxies (Verter & Hodge 1995; Arimoto, Sofue, & Tsujimoto 1996; Wilson 1995) and may overpredict N_{H_2} in galactic centers (Dahmen et al. 1998; Meier & Turner 2001). Our derived N_{H_2} values within the disk of M83 are estimated

² Available at <http://www.tuc.nrao.edu/12meter/obsinfo.html>.

³ See note 2.

to be accurate to within a factor of 2 in the disk, with higher internal relative accuracy. The areas that are most uncertain as a result of X_{CO} are the central beam on the nucleus and the outer edges of the map, which we discuss later. We will adopt the standard conversion factor, $X_{\text{CO}} = N_{\text{H}_2}/I_{\text{CO}} = 2 \times 10^{20} \text{ cm}^{-2} (\text{K km s}^{-1})^{-1}$, of Strong et al. (1988) throughout the remainder of the paper [although we note that the most recent calibration by Hunter et al. 1997 finds a mean $X_{\text{CO}} = 1.6 \times 10^{20} \text{ cm}^{-2} (\text{K km s}^{-1})^{-1}$ for the entire Milky Way disk and $X_{\text{CO}} = 2.7 \times 10^{20} \text{ cm}^{-2} (\text{K km s}^{-1})^{-1}$ for the outer disk, $R > R_0$]. Using this conversion factor, I_{CO} can be converted into molecular gas surface densities via the standard conversion factor using $\Sigma_{\text{H}_2} (M_\odot \text{ pc}^{-2}) = 3.3 I_{\text{CO}} (\text{K km s}^{-1})$ including a correction for inclination, with a systematic uncertainty of about a factor of 2 in the conversion to H_2 .

2.2. VLA H I, 21 cm Continuum, and IRAS Far-Infrared Observations

We obtained archival VLA D and C array 21 cm observations of M83 (originally by Ondrechen & van der Hulst), used in the H I study of M83 by Tilanus & Allen (1993). The naturally weighted cube was corrected for primary beam attenuation. The $46'' \times 26''$ VLA beam was convolved to a $50''$ circular beam for comparison with our 12 m CO (1–0) data. The same clipping procedure described for the CO maps was used to construct the H I integrated intensity map, from data greater than $0.0017 \text{ Jy beam}^{-1}$ (1.2σ). Absolute flux calibration uncertainty is on the order of the uncertainty in the flux calibrator, less than 2%. Integrated intensity was converted to H I surface density using $\Sigma_{\text{H I}} = 3.9 M_\odot \text{ pc}^{-2} (\text{Jy beam}^{-1} \text{ km s}^{-1})^{-1} I_{\text{H I}}$. To estimate the amount of flux missing as a result of the lack of short baselines (emission with size scales greater than $15'$), we compare the total H I flux of 480 Jy km s^{-1} from our VLA map to the H I flux of $1076 \text{ Jy km s}^{-1}$ from a Dwingeloo 25 m single-dish spectrum of M83 (Tilanus & Allen 1993) whose beam matches the primary beam of our VLA map. This indicates that 60% of the H I emission may be missing from the VLA map. From comparisons to $I_{\text{H I}}$ contours in the large ($100'$) H I map made with the Effelsberg 100 m telescope (Huchtmeier & Bohnenstengel 1981) as well as to the Dwingeloo spectrum, we obtain an estimate of $2 \pm 0.5 M_\odot \text{ pc}^{-2}$ for the mean missing H I surface density of features greater than $15'$ in the inner $20'$ disk of M83, or roughly 2 times the lowest contour in the gas surface density map we present.

A 21 cm continuum map was made by averaging the off-line channels (prior to continuum subtraction). The resulting 21 cm continuum map has an rms noise level of $0.7 \text{ mJy beam}^{-1}$.

High-resolution (HiRes) 60 and $100 \mu\text{m}$ IRAS maps were obtained from IPAC.⁴ The enhanced resolution images were produced by 200 iterations of the maximum correlation method. The effective beam is $41'' \times 31''$, P.A. = 119° for the $60 \mu\text{m}$ map and $65'' \times 54''$, P.A. = 121° for the $100 \mu\text{m}$ map. The 1σ noise is 0.8 MJy sr^{-1} in the $60 \mu\text{m}$ map and 0.9 MJy sr^{-1} in the $100 \mu\text{m}$ map.

3. IMAGES OF M83 IN CO: THE MOLECULAR GAS

3.1. CO (1–0) Maps

The 36 channels with CO (1–0) line emission are displayed in Figure 1. The CO (1–0) channel maps show the butterfly pattern of emission expected for a differentially rotating disk. High-velocity gas is seen at the nucleus in all the channels, extending over 180 km s^{-1} (425 km s^{-1} corrected for inclination; see § 5).

The disk of CO emission in M83 extends to a radius of 5.5 (6.4 kpc), as shown in the maps of integrated intensity, $I_{10} = \int T_{10} dv$, and peak main-beam brightness temperature, T_{10} (Fig. 2). While I_{10} represents the total emission at all velocities, T_{10} is in part a measure of the areal filling factor for the CO (1–0) emission in the beam. Both maps show the same features: a bright nucleus, a bar roughly oriented northeast to southwest, and spiral arm structure that starts at the ends of the bar. While $55''$ resolution prevents us from separating arm from interarm CO in the innermost regions of the disk, beyond a $3'$ galactic radius interarm CO can be distinguished. It is clear that the entire inner $11'$ diameter optical disk of M83 is filled with CO-emitting gas.

M83 is known for its prominent bar. The $6'$ long (7 kpc) bar in M83 is also readily apparent in the CO maps. Local maxima in T_{10} are present at the ends of the bar, 0.63 K at the eastern end and two 0.73 K marginally resolved peaks at the western end. Multiple peaks at the western end of the bar were also seen in higher resolution interferometric maps (Kenney & Lord 1991). The mean I_{10} for the clump at the western end of the bar is 28 K km s^{-1} ($\Sigma_{\text{H}_2} = 92 M_\odot \text{ pc}^{-2}$), and it contains $9.1 \times 10^7 M_\odot$ of H_2 gas. The clump at the eastern end of the bar has $\langle I_{10} \rangle = 22 \text{ K km s}^{-1}$ ($\Sigma_{\text{H}_2} = 78 M_\odot \text{ pc}^{-2}$) and contains $7.8 \times 10^7 M_\odot$ of H_2 gas. Throughout the bar region, $I_{10} > 17 \text{ K km s}^{-1}$ ($\Sigma_{\text{H}_2} > 55 M_\odot \text{ pc}^{-2}$) and $T_{10} > 0.36 \text{ K}$. The contrast in I_{CO} between the bar and locations $1'$ off the bar is ~ 2.2 .

Spiral arm structure beyond the bar is apparent in the broad, inverted “S” pattern. Along the spiral arms both I_{CO} and T_{10} are a factor of 3 lower than in the bar. There is an underlying smooth disk of CO (1–0) emission with I_{10} on the order of 3 K km s^{-1} ($\Sigma_{\text{H}_2} \sim 10 M_\odot \text{ pc}^{-2}$). Interferometer maps covering the eastern spiral arm (Rand et al. 1999) show a series of clumps of CO emission along the eastern arm with masses similar to those of large Galactic giant molecular clouds (GMCs) or small Galactic giant molecular associations (GMAs). While the interferometric CO arms are relatively narrow, $\sim 20''$ wide, we find that the interferometric arms recover only $\sim 5\%$ of total CO flux in a $1'$ single-dish beam. Rand et al. (1999) note that molecular gas in M83 may be widespread on scales similar to that of the spiral arms and the galaxy itself, and we confirm this conjecture.

M83 is also known for its bright starburst nucleus, which shows up prominently in our CO maps (Rieke 1976; Bohlin et al. 1983; Trinchieri et al. 1985; Turner et al. 1987; Turner & Ho 1994). The nucleus has a peak value of $I_{10} = 76 \text{ K km s}^{-1}$ or $\Sigma_{\text{H}_2} = 250 M_\odot \text{ pc}^{-2}$ (corrected for inclination). For the 1.2 kpc nuclear region (the $55''$ beam centered on the nucleus) we find a mean $\langle I_{10} \rangle = 76 \text{ K km s}^{-1}$ ($\Sigma_{\text{H}_2} = 250 M_\odot \text{ pc}^{-2}$) and $T_{10} = 0.89 \text{ K}$, and it contains a total molecular mass of $2.5 \times 10^8 M_\odot$. This mass is twice the value found by Handa et al. (1990), $1.3 \times 10^8 M_\odot$, adjusted for X_{CO} and distance for a $30''$ diameter region centered on the nucleus using the Nobeyama Radio Observatory (NRO) 45 m tele-

⁴ A description of IRAS HiRes reduction is available at <http://www.ipac.caltech.edu/ipac/iras/toc.html>.

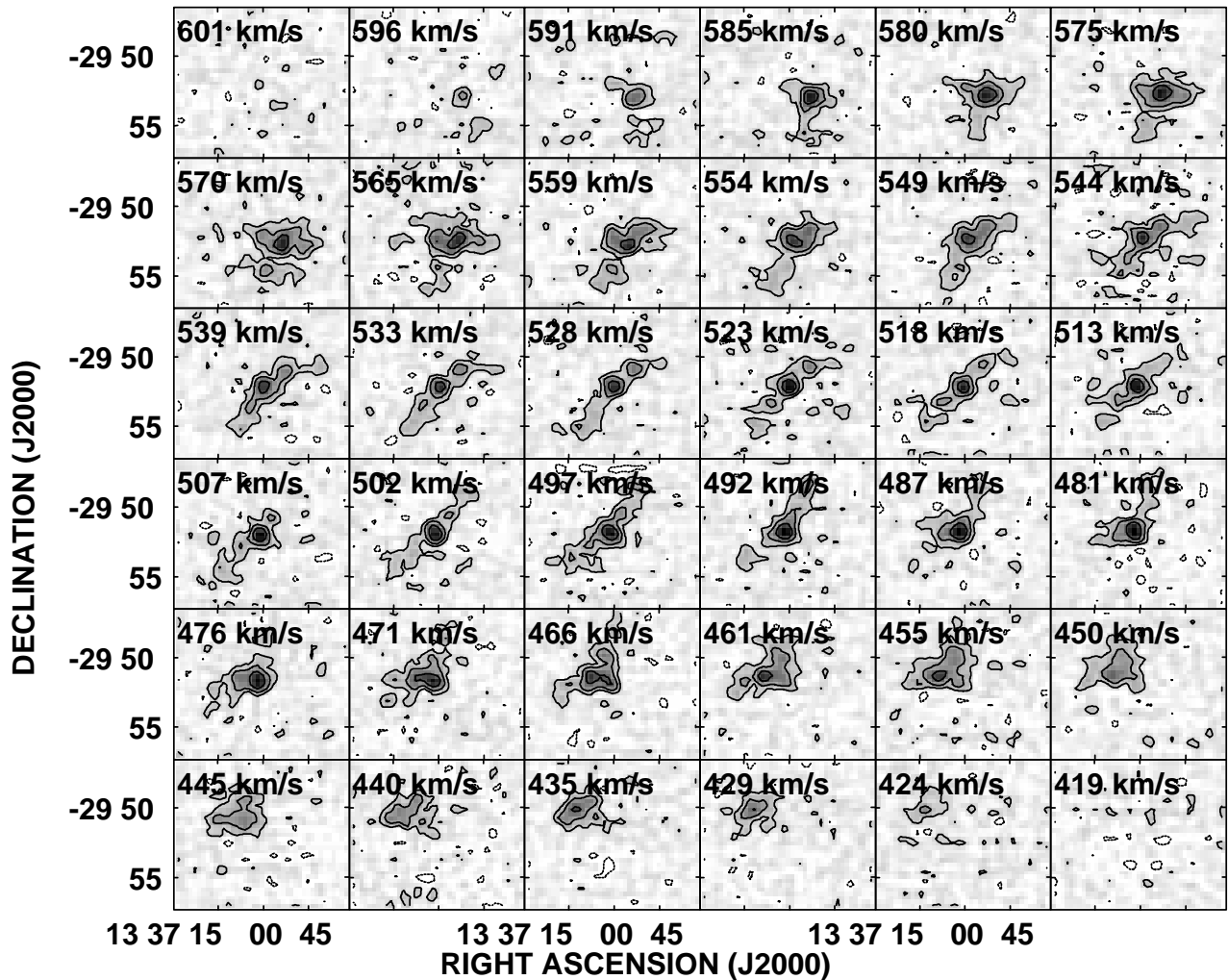


FIG. 1.—CO (1–0) line emission channel maps for M83. Gray scale ranges from 0 to 0.84 K. The rms noise is 0.046 K. Contours are at -0.09 , 0.09 , 0.23 , and 0.46 K. Each channel is labeled with the channel velocity (LSR).

scope with a $16''$ beam. From this we infer that 50% of our nuclear mass value is contained within the central 30% of our $55''$ beam. Converting our total observed I_{10} into a total molecular mass, we obtain $M_{\text{H}_2} = 2.5 \times 10^9 M_{\odot}$ for the total molecular mass of M83, uncertain by a factor of 2 as a result of the uncertainty in X_{CO} .

3.2. CO (2–1) Maps

The 36 channels containing CO (2–1) line emission are displayed in Figure 3. The emission patterns for CO (2–1) are generally the same as that of CO (1–0), with the factor of 2 difference in spatial resolution accounting for most of the difference. Like CO (1–0), high-velocity gas is present at the nucleus, spread across nearly all the channels of the butterfly pattern.

The integrated intensity ($I_{21} = \int T_{21} dv$) and peak main-beam brightness temperature (T_{21}) maps are shown in Figure 4. Taking into account differences in beam size, the CO (2–1) maps look very much like the CO (1–0). This is somewhat surprising. We might expect the interarm component of molecular gas to be colder than arm gas, and not as bright relatively speaking in CO (2–1). The fact that CO (2–1) is nearly as bright suggests that the temperature of the interarm gas is fairly warm, warmer than ~ 4 – 7 K (§ 7).

In CO (2–1) the nucleus and bar are readily seen against an underlying disk of emission. The bright nucleus of M83 is again prominent in the I_{21} map with a peak value of $I_{21} = 133 \text{ K km s}^{-1}$ (the peak T_{21} is 1.8 K). The bar is traced by the 0.53 K contour in the T_{21} map and the 20 K km s^{-1} contour in the I_{21} map. Contrast between the bar and the smoother disk $1'$ off the bar, ~ 2.5 , is similar to the CO (1–0) contrast. Local maxima with $T_{21} = 1.2$ K are again seen at the ends of the bar. The peak I_{21} is 38 K km s^{-1} at the western end of the bar; it is 33 K km s^{-1} at the eastern end.

CO (2–1) emission in M83 extends to a radius of $4'$ (4.7 kpc) nearly as far as does CO (1–0). Spiral arms are seen in a broad, inverted “S” pattern in the CO (2–1) maps. The temperature of the disk of CO (2–1) emission is relatively uniform, $T_{21} \sim 0.4$ – 0.5 K. Not only is there a substantial interarm CO (1–0) component in M83, but we confirm the existence of substantial interarm gas with the higher resolution CO (2–1) data as well.

4. THE TOTAL NEUTRAL GAS DISK OF M83

4.1. H_2 and H I Surface Density

M83 is a molecular gas-rich galaxy. The inner $11'$ (13 kpc) of M83 is dominated by H_2 . At $2.5 \times 10^9 M_{\odot}$, M_{H_2} is 6% of

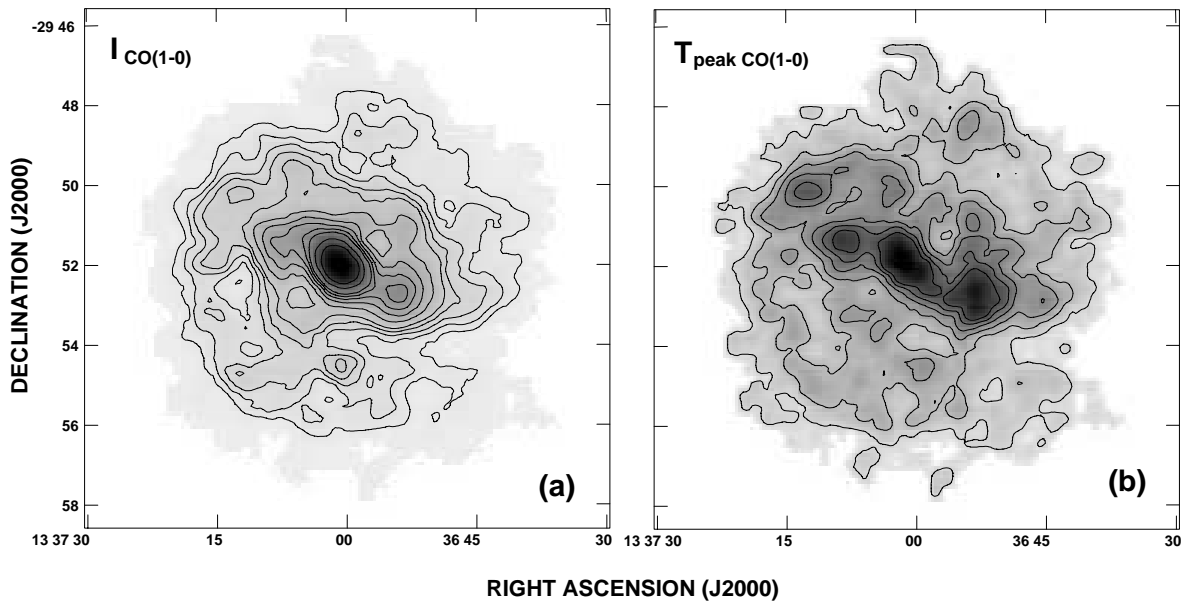


FIG. 2.—CO (1–0) integrated intensity and peak intensity maps for M83. (a) CO (1–0) integrated intensity map. Gray scale ranges from 0 to the peak map intensity, 73 K km s^{-1} . The contour levels are 2, 4, 6, 8, 10, 14, 18, 22, 26, 30, 40, and 50 K km s^{-1} . Intensities can be converted to H_2 column densities using the factor $2 \times 10^{20} \text{ cm}^{-2} (\text{K km s}^{-1})^{-1}$. (b) CO (1–0) peak intensity map. Gray scale ranges from 0 to the peak map intensity, 0.84 K . The contour levels are 0.09, 0.18, 0.27, 0.37, 0.46, and 0.55 K .

the dynamical mass of M83 over the same region. This is 3 times the mean $M_{\text{H}_2}/M_{\text{dyn}}$ for the region containing H_2 in spiral galaxies found by Sage (1993). The mass of H I in the inner $10'$ diameter, roughly the extent of the optical disk, is $5.1 \times 10^8 M_{\odot}$ (without a correction for undersampled flux), 20% of the H_2 mass we have obtained from CO. For the entire $47'$ extent of the M83 disk, the total H I mass is $6.2 \times 10^9 M_{\odot}$ (Huchtmeier & Bohnenstengel 1981, corrected for distance); 30% of the total gas disk mass is molecular. This is consistent with the findings of Young & Knezek (1989), who find $M_{\text{H}_2}/M_{\text{H I}}$ to be a strong function of Hubble type.

Spatial distributions of CO and H I are compared in Figure 5. The H I emission has a small $2'$ central hole. The H I hole is filled with CO emission. However, aside from a general radial trend for the inner disk gas to be molecular rather than atomic, the H I and CO are actually well correlated outside of the central hole. A pattern of $\text{H I}/\text{CO}$ spiral arms begins at the leading ends of the CO bar (assuming trailing spiral arms). The $\text{H I}/\text{CO}$ arms bifurcate at these points with one arm at a low pitch angle ($\sim 10^\circ$) and the other arm extending radially outward $\sim 2'$ before assuming a pitch angle similar to the other arm. At a radius of $4/5$ (5 kpc), roughly the optical extent, emission levels of both CO and H I fall off sharply and the well-defined gas spiral arm pattern terminates. This sharp gas transition is coincident with the onset of significant warping of M83's disk (Rogstad et al. 1974). Disk H I emission continues to larger radii but at emission levels reduced by an average factor of ~ 3.5 compared to the mean of the inner disk.

Figure 6 is a false color image of H I and CO emission in M83. The color balance is set so that the regions of overlap of the H I (red) and CO (green) are orange at a column density of $N_{\text{H}_2} \sim 2.5N_{\text{H I}} \sim 2 \times 10^{21} \text{ cm}^{-2}$. The CO bar region is enhanced by including a blue channel for $N_{\text{H}_2} > 4 \times 10^{21} \text{ cm}^{-2}$. The striking points about this image are (1) the size-

able CO/ H I overlap region, (2) the sharp falloff in both CO and H I at $6'$ (7 kpc), and (3) the intricate ringlike structure of the atomic disk beyond $6'$.

The total neutral gas surface density map, $\Sigma_{\text{gas}} = 1.36(\Sigma_{\text{H I}} + \Sigma_{\text{H}_2})$ (corrected for inclination), is presented in Figure 7 in gray scale and contours. Σ_{gas} varies from a peak, $340 M_{\odot} \text{ pc}^{-2}$, at the nucleus out to less than $1 M_{\odot} \text{ pc}^{-2}$ at the extremities of the H I disk. Molecular gas dominates Σ_{gas} ($\Sigma_{\text{H}_2} > 5\Sigma_{\text{H I}}$) in the inner $9'$ gas disk, where $\Sigma_{\text{gas}} > 10 M_{\odot} \text{ pc}^{-2}$.

Azimuthally averaged H_2 , H I , and neutral gas densities as a function of galactic radius are shown in Figure 8. H_2 and H I reach equal surface density at a radius of $5'$ (6 kpc), at the radius of the sharp falloff in gas surface density.

4.2. CO, Gas, and Star Formation Tracers: Morphology Comparisons

As the precursor to star formation, CO should be strongly correlated with tracers of ongoing formation of massive stars. Blue optical images trace the locations of recent massive star formation. Far-infrared (FIR) emission traces dust heated by the interstellar radiation field from predominantly young blue stars in its proximity. On these size scales one might thus expect to see a correlation of FIR and CO emission. The 21 cm continuum is a tracer of nonthermal emission from relativistic electrons accelerated by supernova remnants (SNRs), an end state for the short-lived massive stars that early on caused the FIR emission.

R. Tilanus kindly provided a *B*-band optical image that we compare to the CO (1–0) emission in Figure 9. Inside corotation ($R \sim 2/4$, 3 kpc; Kenney & Lord 1991), knots of blue emission outline the leading edge of the CO bar and arms. Clumps of CO emission lie at the ends of the optical bar. It is tempting to interpret this pattern of emission at the ends of the bar in terms of the model for orbit crowding and

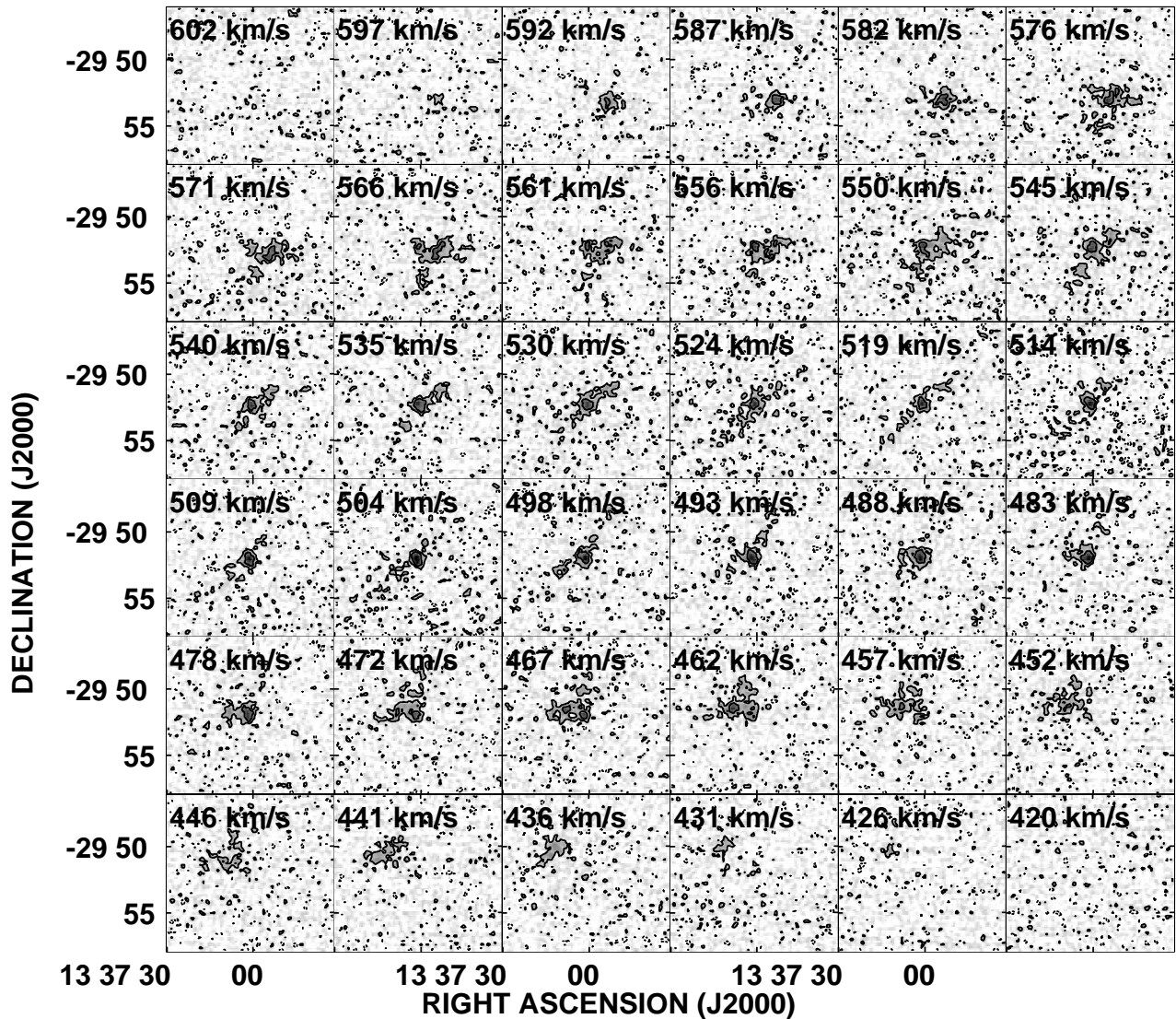


FIG. 3.—CO (2–1) line emission channel maps for M83. Gray scale ranges from 0 to 1.7 K. The rms noise in a channel with no emission is 0.133 K. Contours are at -0.27 , 0.27 , and 0.66 K. Each channel is labeled with the channel velocity (LSR).

shock focusing presented by Kenney & Lord (1991). While the CO emission generally follows the blue light pattern, the ratio of I_{CO} to blue optical emission increases by a factor of 8 from the highest to the lowest I_{CO} regions. This anticorrelation is consistent with findings of Sage & Solomon (1989), who find blue light to be an unreliable tracer of recent star formation due to extinction.

The locations of H II regions, from H α observations (Rumstay & Kaufman 1983), relative to the CO disk are shown in Figure 10a. While the H α extinction is high in M83 as a result of a uniform screen of dust, the apparent distribution of H α emission is not a result of differential extinction across bar and arm features in M83 (Rumstay & Kaufman 1983; Lord & Kenney 1991; Tilanus & Allen 1993; Rand et al. 1999). The leading edge of the CO bar and spiral arm pattern is traced by the H II regions, like the blue light. This is consistent with a general scenario in which gas flows into the trailing bar/arm pattern (clockwise for M83) and accumulates molecular gas in the bar/arm potential well, causing elevated star formation as a temporally and spatially delayed product as material moves through the

bar/arm pattern. There is no clear correlation between the number density of H II regions and I_{10} on these size scales. There are regions of significant CO but little H α ($\alpha = 13^{\text{h}}37^{\text{m}}5^{\text{s}}$, $\delta = -29^{\circ}53'$) and regions with H α and little CO ($\alpha = 13^{\text{h}}36^{\text{m}}55^{\text{s}}$, $\delta = -29^{\circ}48'$)! The density of H II regions relative to I_{10} appears to be higher along the outer arm pattern than along the bar itself, although this may be due to extinction of H α along the gas-rich bar.

An excellent morphological correlation between 21 cm continuum and CO (1–0) emission in M83 is seen in Figure 10b. This kind of correlation is also seen in IC 342 (Crosthwaite et al. 2001). We might nominally expect the radio continuum to be more closely associated with the pattern of H II regions seen in Figure 10a, in effect tracing the location of recent, short-lived, massive star formation, the source of cosmic-ray electrons that produce nonthermal continuum. However, the 21 cm continuum contours clearly show a better correlation to the molecular gas. This correlation underscores the importance of gas density and associated magnetic fields in the extraction of synchrotron emission from cosmic rays that diffuse from their source

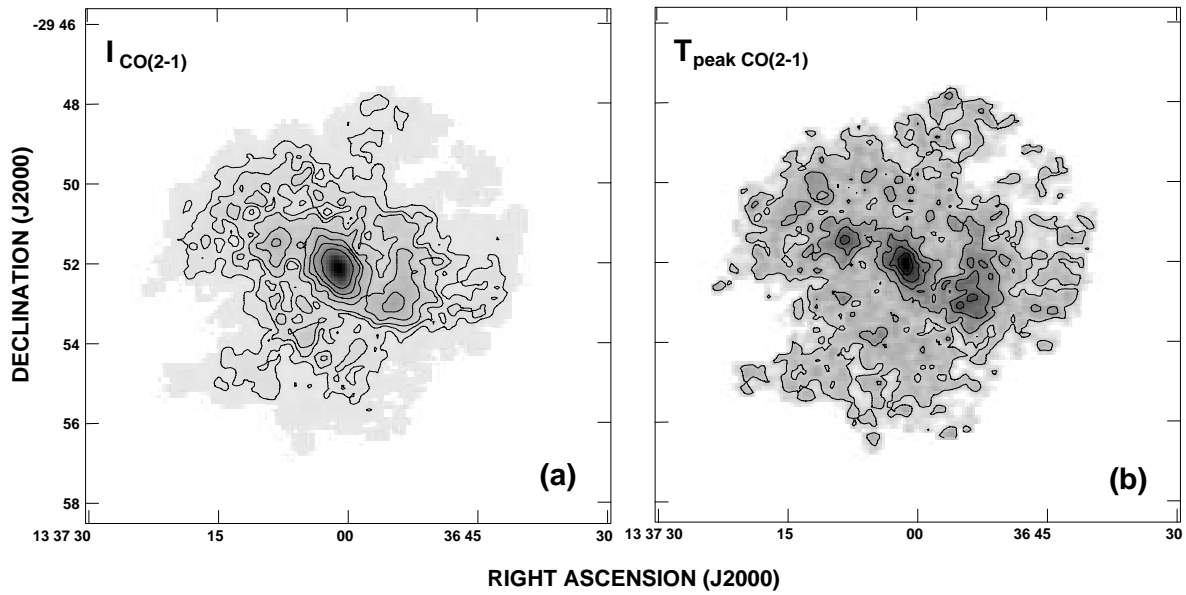


FIG. 4.—CO (2–1) integrated intensity and peak intensity maps for M83. (a) CO (2–1) integrated intensity map. Gray scale ranges from 0 to the peak map intensity, 133 K km s^{-1} . The contour levels are 4, 8, 12, 20, 30, 40, and 60 K km s^{-1} . (b) CO (2–1) peak intensity map. Gray scale ranges from 0 to the peak map intensity, 1.7 K . The contour levels are 0.27, 0.53, 0.80, 1.06, and 1.33 K .

with a characteristic $\sim 1 \text{ kpc}$ scale length (Bicay, Helou, & Condon 1989; Bicay & Helou 1990; Helou & Bicay 1993). However, the separation between the major axis of the CO bar and the ridge of H II regions is less than the CO beamwidth, and the lack of a CO/21 cm offset may be due to the $1'$ resolution data used in the comparison.

Another explanation for the correlation of CO and 21 cm continuum is the heating of molecular clouds by cosmic rays (Adler, Allen, & Lo 1991; Allen 1992; Suchkow, Allen, & Heckman 1993). Our observations are consistent with this scenario.

CO and FIR comparisons are shown in Figures 10c and 10d. Given that the correlation of H II regions and CO is fairly good, we might expect to see similar correlations between CO (1–0) and $100 \mu\text{m}$ FIR (Fig. 10c) as well as CO (2–1) and $60 \mu\text{m}$ FIR (Fig. 10d), each pair respectively tracing cooler versus warmer gas and dust.

Despite the expected correlation between molecular gas and dust heated by ongoing star formation, CO and FIR are not as well correlated as CO/21 cm continuum, particularly along the bar. The lack of a good CO/FIR correlation was also found by Sodroski et al. (1994) for the Galaxy.

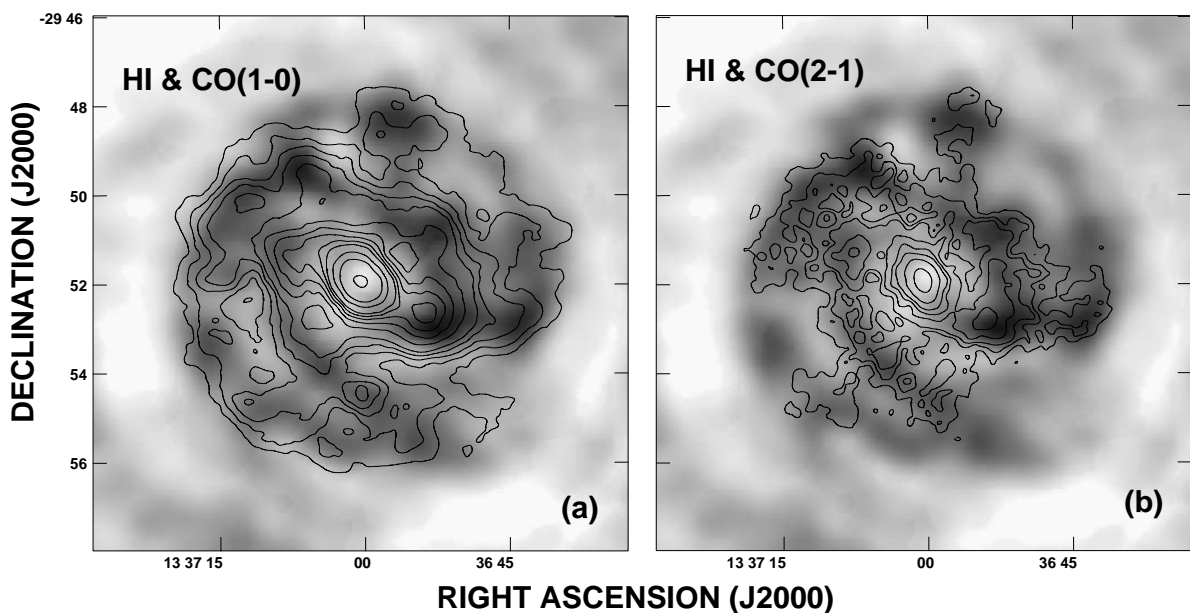


FIG. 5.—CO and H I in M83. (a) $I_{\text{H I}}$ (gray) and I_{10} (contours). Gray scale ranges from 0 to $2.6 \text{ Jy beam}^{-1} \text{ km s}^{-1}$. The I_{10} contours are at 2, 4, 6, 8, 10, 14, 18, 22, 26, 30, 40, 50, and 70 K km s^{-1} . (b) $I_{\text{H I}}$ (gray) and I_{21} (contours). Gray scale ranges from 0 to $3.7 \text{ Jy beam}^{-1} \text{ km s}^{-1}$. The I_{21} contours are at 4, 8, 12, 20, 30, 40, 60, and 100 K km s^{-1} .

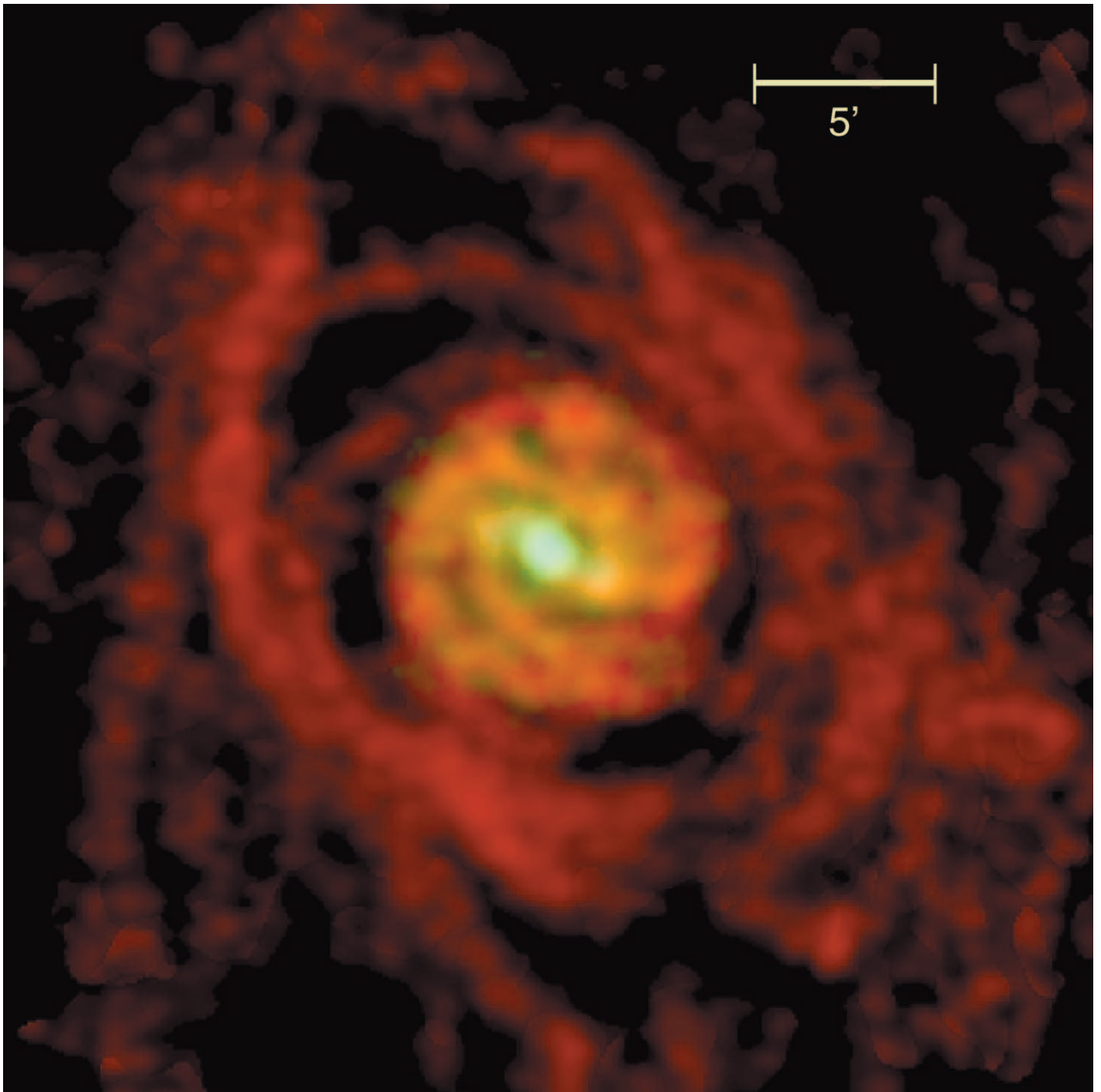


FIG. 6.— $I_{\text{CO}}/I_{\text{H I}}$ comparison for M83. I_{CO} is shown in green. $I_{\text{CO}} > 20 \text{ K km s}^{-1}$ is also shown in blue in order to emphasize the molecular bar. $I_{\text{H I}}$ is shown in red. Regions of $I_{\text{CO}}/I_{\text{H I}}$ overlap, where the molecular and atomic gas phases are at surface densities of $N_{\text{H}_2} \sim 2 \times 10^{21} \text{ cm}^{-2}$ and $N_{\text{H I}} \sim 8 \times 10^{20} \text{ cm}^{-2}$, appear in orange.

They suggest that atomic clouds contribute much of the FIR emission. While the overall distributions of CO (1–0) and $100 \mu\text{m}$ are similar, the $100 \mu\text{m}$ bar is conspicuously displaced by $\sim 20^\circ$ counterclockwise from the CO, with CO along the leading edge of the bar (assuming a trailing spiral pattern). This is also true of the total gas surface density. The ridge of H II regions seen in Figure 10a lies between the major axes of the CO and $100 \mu\text{m}$ bars. A possible explanation for the offset is that star formation from molecular

clouds is followed downstream by dust heating (and photo-dissociation) from the radiation fields of the stars as gas moves through the bar. The CO (2–1) emission and $60 \mu\text{m}$ emission show a better spatial correlation without the offset, perhaps because they preferentially trace a warmer component of gas and dust. These correlations and displacements do not disappear when the emission maps are convolved to a larger beam ($70''$). While some distinct shifts are present in Figure 10d, we are reluctant to attribute too much signifi-

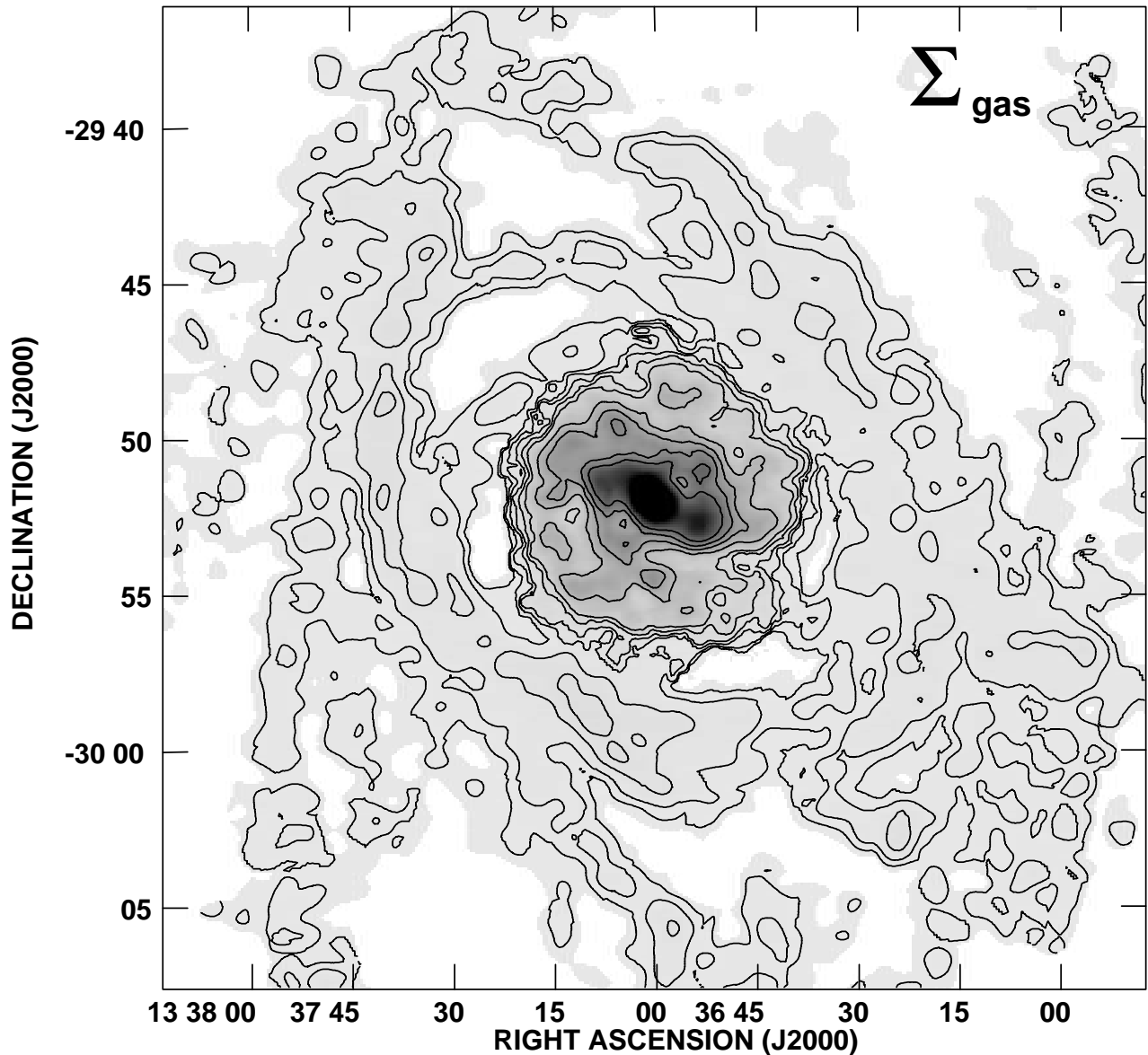


Fig. 7.—Neutral gas surface density in M83. The total neutral gas surface density, $\Sigma_{\text{H}_2} + \Sigma_{\text{H I}}$, is corrected for inclination (25°) and increased by a factor of 1.36 for He content. Gray scale ranges from 0 to $150 M_\odot \text{pc}^{-2}$, and the peak is $328 M_\odot \text{pc}^{-2}$. Contours are at 1, 2, 4, 6, 10, 15, 30, 45, 60, and $80 M_\odot \text{pc}^{-2}$.

cance to small displacements in the FIR because of the possibility of artifacts produced in the HiRes data reduction.⁵

The maps were convolved to a common $70''$ beam size and converted to Jy beam^{-1} units to form the radial plots in Figure 11. The ratio of I_{10} to 21 cm continuum as a function of galactocentric radius is shown in Figure 11a. Despite the scatter ($\sim 10\%$ dex), the ratio is relatively flat between $1'$ and $5'$, which is consistent with the excellent spatial correlation seen in Figure 10b. The scatter is only marginally reduced ($\sim 0.5\%$ dex) when Σ_{gas} instead of CO is compared to 21 cm continuum (Fig. 11b). We do not get the large reduction in scatter ($\sim 35\%$ dex) that we see going from $I_{10}/21$ cm to $\Sigma_{\text{gas}}/21$ cm in another starburst galaxy, IC 342 (Crosthwaite et al. 2001). However, this is more a reflection of the domi-

nant presence of molecular gas in the inner $10'$ of M83 than any breakdown in the excellent $\Sigma_{\text{gas}}/21$ cm continuum correlation.

The displacement of the CO and $100 \mu\text{m}$ bar is seen in Figure 11c as the larger scatter (times 1.5) compared to $F_{I_{10}}/F_{21 \text{ cm}}$ between $1'$ and $3'$. The ratios $F_{I_{10}}/F_{100 \mu\text{m}}$ and $F_{I_{21}}/F_{60 \mu\text{m}}$ peak at ~ 1.5 and decline at larger radii (Figs. 11c and 11d). The decline in $F_{I_{10}}/F_{100 \mu\text{m}}$ and $F_{I_{21}}/F_{60 \mu\text{m}}$ outside of the inner $1.5'$ can be explained in terms of a decline in the fraction of the interstellar medium (ISM) in molecular form that falls from 90% at $1.5'$ to 20% at $5'$. Inside $1.5'$ we interpret the declining ratios as indicating increased star formation rate per unit CO in the vicinity of the starburst nucleus. In summary, we find that the best spatial correlation between gas and a star formation tracer in M83 is found in a comparison of Σ_{gas} and 21 cm continuum; alternatively, I_{10} and 21 cm correlate well because the inner gas disk is primarily molecular.

⁵ See discussion of HiRes artifacts at http://www.ipac.caltech.edu/ipac/iras/hires_artifacts.html.

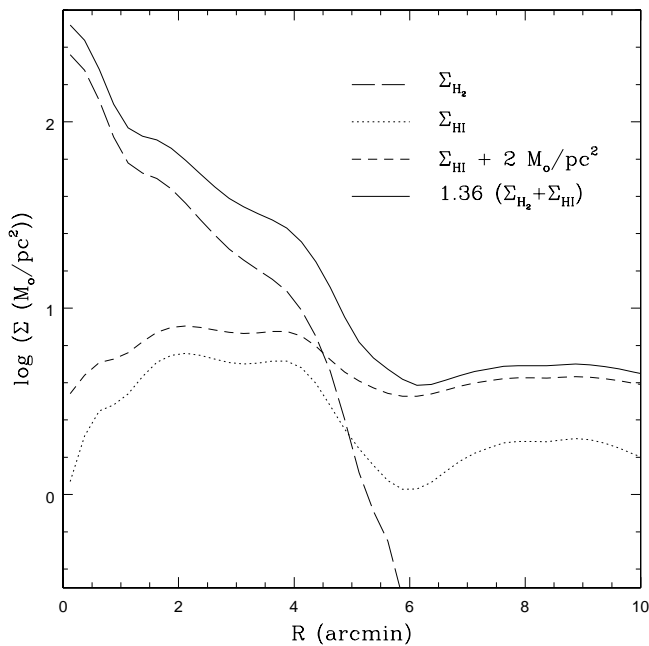


FIG. 8.—Surface density vs. radius in M83. Plotted are Σ_{H_2} derived using a constant, standard conversion factor; $\Sigma_{\text{H I}}$ from the observed emission; the total gas surface density increased by a factor of 1.36 to include the He content; and the total gas surface density including an estimate of the missing H I flux. All have been corrected for inclination (25°).

4.3. CO, Gas, and Star Formation Tracers: The Azimuthal Distribution and the Spiral Pattern

To examine the relationship between the neutral gas components and continuum emission in greater detail, we produced polar maps of various constituents that were corrected to a face-on inclination. All the maps were convolved to match the CO (1–0) $55''$ beam and are presented in Figure 12, with north at 0° azimuth increasing azimuthally counterclockwise.

The molecular bar is apparent in all the polar plots, and especially in CO (Fig. 12*a*), with the exception of H I (Fig. 12*b*). The eastern portion of the bar begins at $\phi \sim 40^\circ$, and the western portion is at $\phi \sim 220^\circ$. The bar is asymmetric and extends to an ~ 2.5 (3 kpc) radius. A clump of strong emission at the western end of the bar ($R \sim 1.7$, $\phi \sim 250^\circ$) appears in all constituents, including H I. Local maxima occur at both ends of the bar ($R \sim 1.7$, $\phi \sim 70^\circ$ and 250°) in the 21 cm (Fig. 12*e*) and $60 \mu\text{m}$ (Fig. 12*f*) maps.

The complex, bifurcating, spiral arm pattern in M83 is also evident in Figure 12. Two spiral arms appear to start at the ends of the bar ($R \sim 2.2$, $\phi \sim 75^\circ$ and 250°), and they wind through 40° in azimuth at a high pitch angle, extending out to $5'$ ($\phi \sim 110^\circ$ and 290°). A second pair of lower pitch angle arms start at the ends of the bar ($R \sim 1.8$, $\phi \sim 80^\circ$ and 275°) and wind through 70° in azimuth, bifurcating at $R \sim 2.5$, $\phi \sim 150^\circ$ and 330° , where the pitch angle then increases for each of the new arms. This outer gas arm structure is most easily seen in the H I plot (Fig. 12*b*). Spiral arm structure is only faintly traced in the diffuse 21 cm continuum plot and the patchy $60 \mu\text{m}$ plot (Figs. 12*e* and 12*f*).

While the global morphology of the bar and arms on kiloparsec-sized scales is similar for CO, H I, and stars, the emission patterns are not necessarily coincident. To quantify offsets, slices through polar plots between $R = 1.5$ and $5'$ in

0.5 increments were made and are presented in Figure 13. These slices correspond to the brightness at a fixed radius as a function of azimuth, ϕ . There are roughly 10 independent beam elements spread across 360° in azimuth at $R \sim 1.5$ changing linearly to 34 independent beams at $R \sim 5'$. Although M83 is a strongly barred galaxy with a well-defined structure, it is not easy to trace spiral structure in the gas. We are hampered by large beams. The correlations between the emission profiles are not always clear. Sometimes the blue optical profile leads the CO, sometimes it is coincident. Sometimes there are multiple blue peaks on either side of a CO or H I feature (see the $R \sim 5'$ plot). In the $R \sim 2.5$ plot, the blue arm at $\phi \sim 50^\circ$ is split into two with all the other tracers coincident, while the arm at $\phi \sim 275^\circ$ has a leading blue profile. Nevertheless, some trends are evident.

The 1.5 and $2'$ azimuthal profiles are dominated by the bar structure in M83. Gas along the bar will enter the bar pattern from the left in these plots. CO peaks at the optical bar or upstream from it. The H I and 21 cm continuum follows the CO although the H I is more extended, with emission appearing upstream as well as on the bar arm. Asymmetries between the eastern and western ends of the bar appear in all the emission profiles.

The emission at 2.5 and $3'$ begins to show the effects of the bifurcating arm pattern. CO and H I profiles generally follow each other with the 21 cm continuum reflecting a combination of both. At $R \sim 2.5$ the CO, H I, and 21 cm profiles are still offset to the concave side of the optical spiral arm pattern by $\phi \sim 10^\circ$ – 20° , indicating that the gas is still inside of the corotation radius at $R \sim 2.5$, since the gas is “catching up” with the spiral density wave (beyond the corotation radius, gas will be passed by the spiral pattern). These offsets begin to disappear by $R \sim 3'$, suggesting that the corotation radius may be close to $R \sim 3'$ (3.5 kpc), consistent with the 2.4 (3 kpc) value cited by Kenney & Lord (1991).

Between 3.5 and $5'$ radius, on scales of $\phi \sim 10^\circ$, CO and H I appear upstream and downstream of the optical arms, on the optical arms or at a minimum on the arms, with no clear pattern of offsets. Moreover, 21 cm continuum still appears to follow the total gas pattern. By 4.5 the optical arm pattern is two armed, although these arms are asymmetric, with a narrow northern feature at $\phi \sim 270^\circ$ caused by the large northern clump.

Throughout these profiles we are able to identify distinct patches of interarm CO in the minima of the optical profile. Prominent examples are (1) in the 2.5 slice at $\phi \sim 140^\circ$ and 310° ($N_{\text{H}_2} = 20 \times 10^{20}$ and $29 \times 10^{20} \text{ cm}^{-2}$, respectively) and (2) in the $4'$ slice at $\phi \sim 50^\circ$, 230° , and 295° ($N_{\text{H}_2} = 7 \times 10^{20}$, 8×10^{20} , and $13 \times 10^{20} \text{ cm}^{-2}$, respectively). These all represent greater than 5σ detections in the I_{CO} map and are separated from optical peaks by over one beamwidth.

4.4. A Comparison to the Barred Spiral Galaxies, IC 342, and the Galaxy

We made a similar neutral gas map for the weakly barred Scd galaxy, IC 342 (Crosthwaite et al. 2001). Both M83 and IC 342 have extensive H I disks, $80'$ and $90'$ in diameter on the sky, respectively (Huchtmeier & Bohnenstengel 1981; Rots 1979). Both galaxies have observed CO disks significantly smaller than their H I diameters, on the order of 10%–15%. The decrease in H I column density in the center

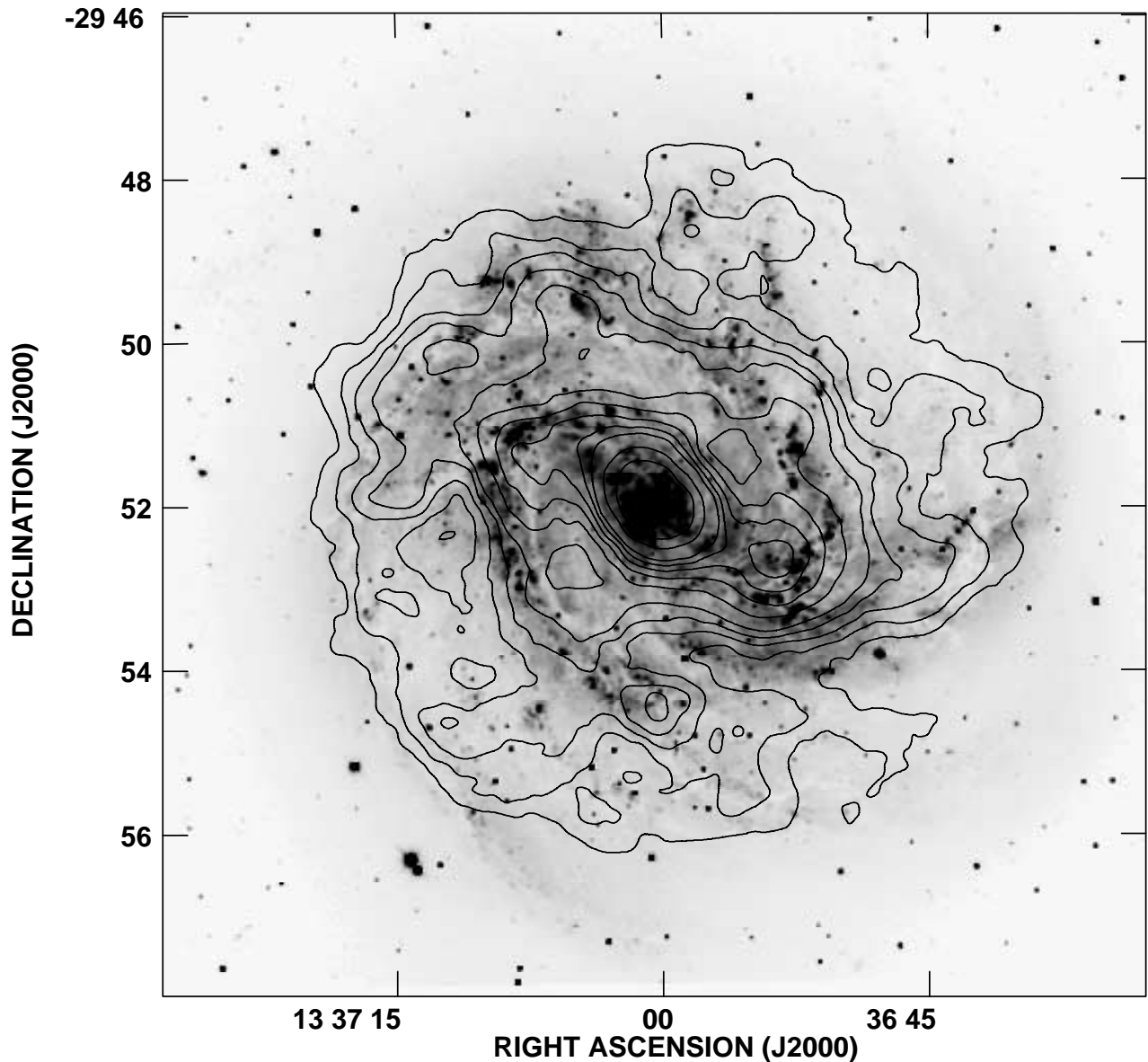


FIG. 9.—M83 optical and CO morphology comparison. The B -band optical image is in gray scale (provided by R. Tilanus) with I_{10} contours at 2, 4, 6, 8, 10, 14, 18, 22, 26, 30, 40, and 50 K km s^{-1} .

of these galaxies, their H I “holes,” occurs at similar radii, 3 kpc ($5'$) in IC 342 and 2.5 kpc ($2'$) in M83. Their H_2 disks have roughly the same radii, 5–6 kpc. Their D_{25} optical diameters are 13 kpc ($11.2'$) for M83 and 10 kpc ($17.8'$) for IC 342 (de Vaucouleurs, de Vaucouleurs, & Corwin 1976) (although IC 342 is in the plane of avoidance, and its unextincted optical diameter may actually be larger).

Much of the similarity ends here. IC 342 (Scd) has a smaller fraction of molecular gas than the earlier type M83 (SBc): the total molecular mass of IC 342, $M_{\text{H}_2} = 7 \times 10^8 M_{\odot}$, is only 25% that of M83, while they have similar dynamical masses. IC 342 also has less atomic gas: the total H I mass of IC 342 is 30% that of M83's H I mass. These results are consistent with the findings of Young & Knezek (1989), Sage (1993), and Young et al. (1995) that early-type spirals tend to have higher $M_{\text{H}_2}/M_{\text{H I}}$. The diameter over which $\Sigma_{\text{H}_2} > 10 M_{\odot} \text{pc}^{-2}$ is 10 kpc for M83, nearly twice

that of IC 342 (6 kpc), while their optical diameters are nearly the same. In M83, Σ_{H_2} falls rapidly to $1 M_{\odot} \text{pc}^{-2}$ by $R \sim 6$ kpc ($5.3'$), a radial span of 1 kpc. The decline is more gradual in IC 342, occurring over a radius of 2.5 kpc, reaching $1 M_{\odot} \text{pc}^{-2}$ at $8'$ (5 kpc). The mean surface density at the nucleus of M83 is 50% higher than in IC 342, despite the smaller linear scale for the $1'$ beam on IC 342. The mean surface density for the disk of IC 342, outside the $1'$ nucleus, is half the value of M83, which is $26 M_{\odot} \text{pc}^{-2}$. M83 has a more massive, hard-edged, molecular disk than IC 342. Perhaps this is related to whatever disturbance caused the warped, disturbed appearance of the outer H I disk of M83, which may also be responsible for the nuclear starburst and the bar.

It is also instructive to compare M83 to the Galaxy, which is probably of Sb Hubble type. The total H_2 mass of the Galaxy and M83 is nearly the same. The H I mass of the Galaxy

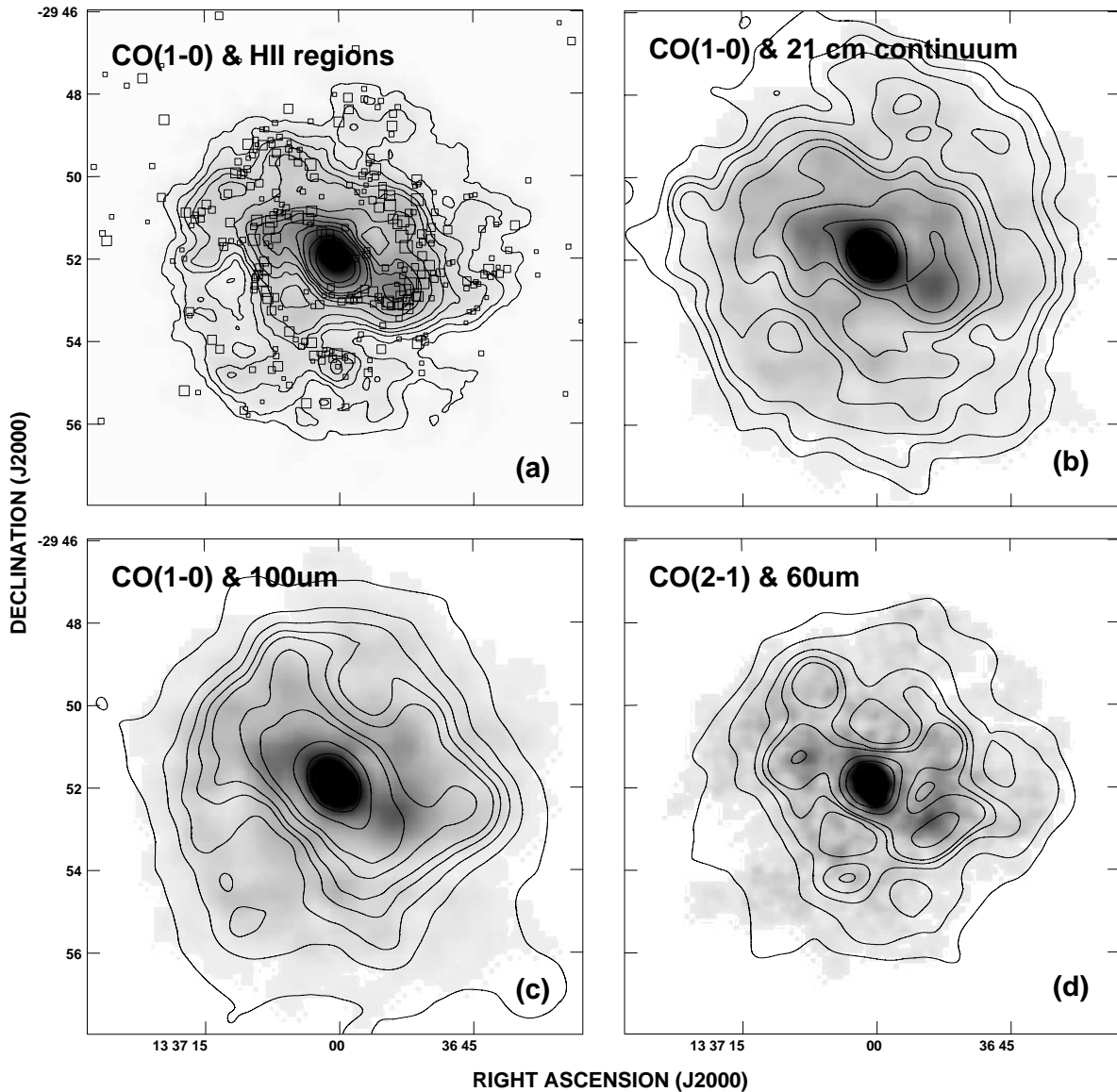


FIG. 10.—CO and star formation tracers in M83. (a) I_{10} in gray scale and contours with the locations of H II regions indicated by open squares. The gray scale ranges from 0 to 57 K km s⁻¹. The contour levels are 2, 4, 6, 8, 10, 14, 18, 22, 26, 30, 40, and 50 K km s⁻¹. The H II regions are from the list by Rumstay & Kaufman (1983). The squares range in size based on the total H α flux from the region. The smallest squares represent $\log S_{\text{H}\alpha} = -14$ and the largest -11 , with $S_{\text{H}\alpha}$ in ergs cm⁻² s⁻¹. (b) I_{10} in gray scale with 21 cm continuum contours. The gray scale ranges from 0 to 43 K km s⁻¹. The 21 cm contours are at 1.4, 2.8, 4.2, 7, 10.5, 14, 21, 35, and 70 mJy beam⁻¹. The beam size (FWHM) is 45" \times 45", P.A. = 73°, and the rms noise level is 0.7 mJy beam⁻¹. (c) I_{10} in gray scale with IRAS 100 μ m contours. The gray scale ranges from 0 to 43 K km s⁻¹. The 100 μ m contours are at 20, 40, 60, 80, 100, 150, 200, 400, and 600 MJy sr⁻¹. The beam size (FWHM) is 65" \times 54", P.A. = 20°, and the rms noise level is 2 MJy sr⁻¹. (d) I_{21} in gray scale with IRAS 60 μ m contours. The gray scale ranges from 0 to 56 K km s⁻¹. The 60 μ m contours are at 30, 40, 60, 80, 100, 200, and 400 MJy sr⁻¹. The beam size (FWHM) is 41" \times 31", P.A. = 21°, and the rms noise level is 0.6 MJy sr⁻¹.

is 75% that of M83, despite the fact that the Galaxy is ~ 3 times more massive than M83 (Kulkarni & Heiles 1987; Combes 1991; Young & Scoville 1991). The mean surface density of nonnuclear H₂ in M83 is 7 times that of the Galaxy (Scoville & Sanders 1987). M83 lacks the prominent H₂ ring of Σ_{H_2} found in the Milky Way (Clemens, Sanders, & Scoville 1988), although the edge of the Galactic ring and the edge of the CO disk in M83 are both at 6 kpc. The results are consistent with findings that early-type spirals tend to have higher $M_{\text{H}_2}/M_{\text{H I}}$ (Young & Knezek 1989; Sage 1993; Young et al. 1995).

In short, M83 appears to be molecular gas-rich, even more so than typical for its Hubble type. This distribution

and fraction of the gas disk in molecular form found in M83 are not found in the less strongly barred Scd galaxy IC 342.

5. THE GAS KINEMATICS OF M83

Intensity-weighted velocity maps for CO (1–0), CO (2–1), and H I are presented in Figure 14. The “spider” pattern characteristic of an inclined rotating disk can be seen in the CO velocity maps and the inner 9' of the H I velocity map, although both of the CO velocity maps show departures from circular rotation.

At the edges of the CO (1–0) velocity map, the effect of severe warping can be seen as a counterclockwise rotation

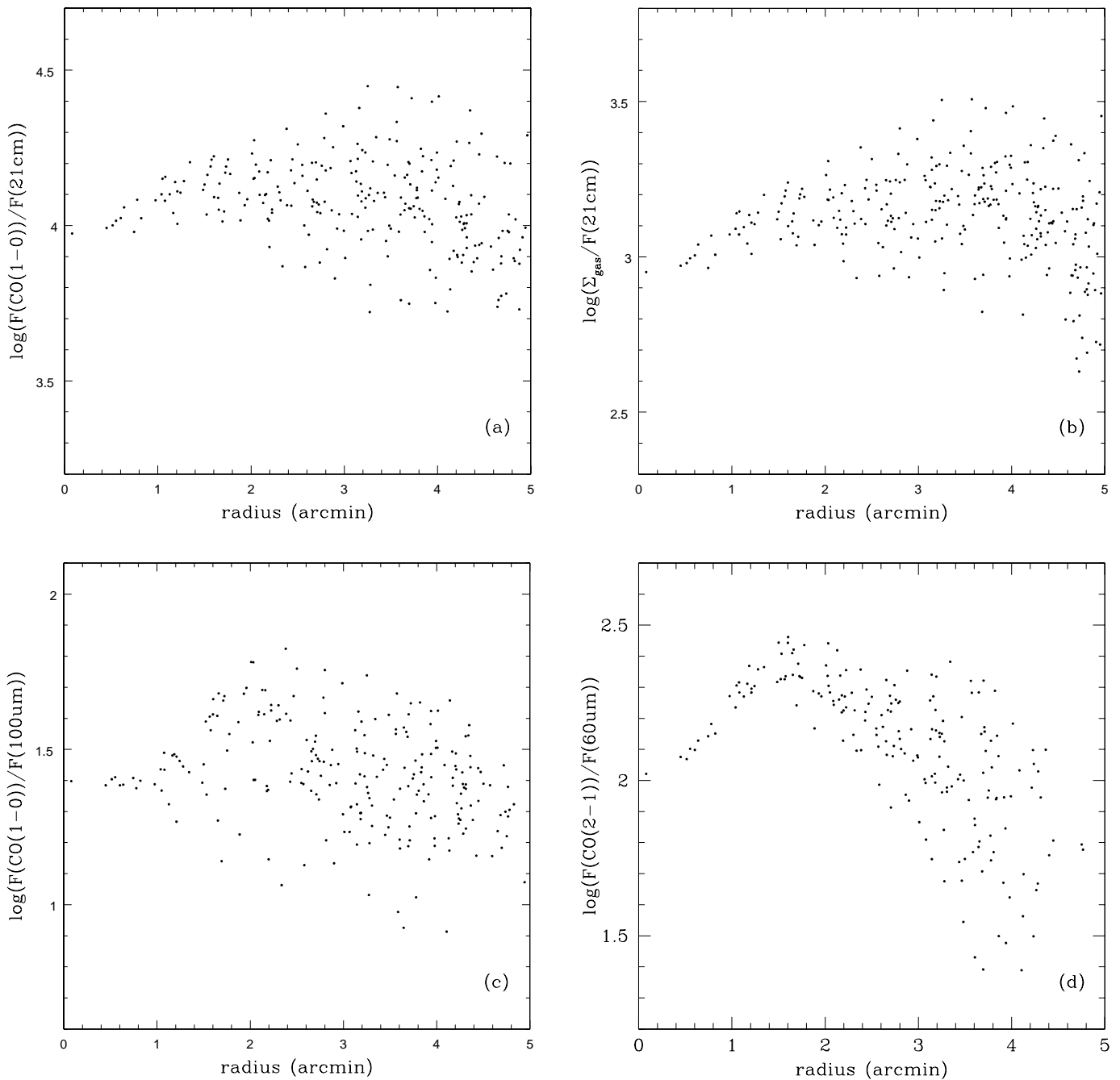


FIG. 11.—Radial trends in the star formation tracers. (a) Ratio of CO (1–0) line emission to 21 cm continuum. (b) Ratio of total gas surface density, Σ_{gas} , to 21 cm continuum. (c) Ratio of CO (1–0) line emission to 100 μm . (d) Ratio of CO (2–1) line emission to 60 μm . The emission maps were convolved to a $70''$ FWHM beam size and clipped at a 4σ level prior to forming the ratios. The μm emission was converted to Jy beam^{-1} units and I_{CO} to $\text{Jy beam}^{-1} \text{ km s}^{-1}$.

of the isovelocity contours. The H I velocity map outside of the inner $9'$ contains even stronger signatures of severe warping in the outer region (Rogstad et al. 1974). The warping of the H I layer starting where the stellar disk comes to an abrupt edge is a common feature of warped galactic disks (Sparke & Casertano 1988; Christodoulou, Tohline, & Steiman-Cameron 1993). Modeling has shown that the type of warp seen in M83 can be caused by triaxial galactic halo if the disk orbits the short axis of the halo and the core radius of the halo is small relative to the disk scale length (Sparke 1984a, 1984b; Sparke & Casertano 1988).

The location of the bar should be reflected in the CO (1–0) and H I intensity-weighted velocity dispersion maps (σ_{CO} ,

$\sigma_{\text{H I}}$) of Figure 14 because we expect streaming motions along the bar as seen in IC 342 (Crosthwaite et al. 2001). The bar in M83 is indeed traced by higher $\sigma_{\text{H I}}$. The bar is less apparent in σ_{CO} , although higher σ_{CO} values do appear at the ends of the bar.

The pattern of higher σ_{CO} and $\sigma_{\text{H I}}$ perpendicular to the bar major axis seen in Figure 14 is unexpected. This pattern suggests that radial perturbations are present, since these are more easily detected along the minor axis. Strong radial gradients are not expected in this interarm region. To eliminate any velocity artifacts resulting from our viewing angle, we modeled the component of dispersion that is due to galactic rotation within a $55''$ beam. This component peaks

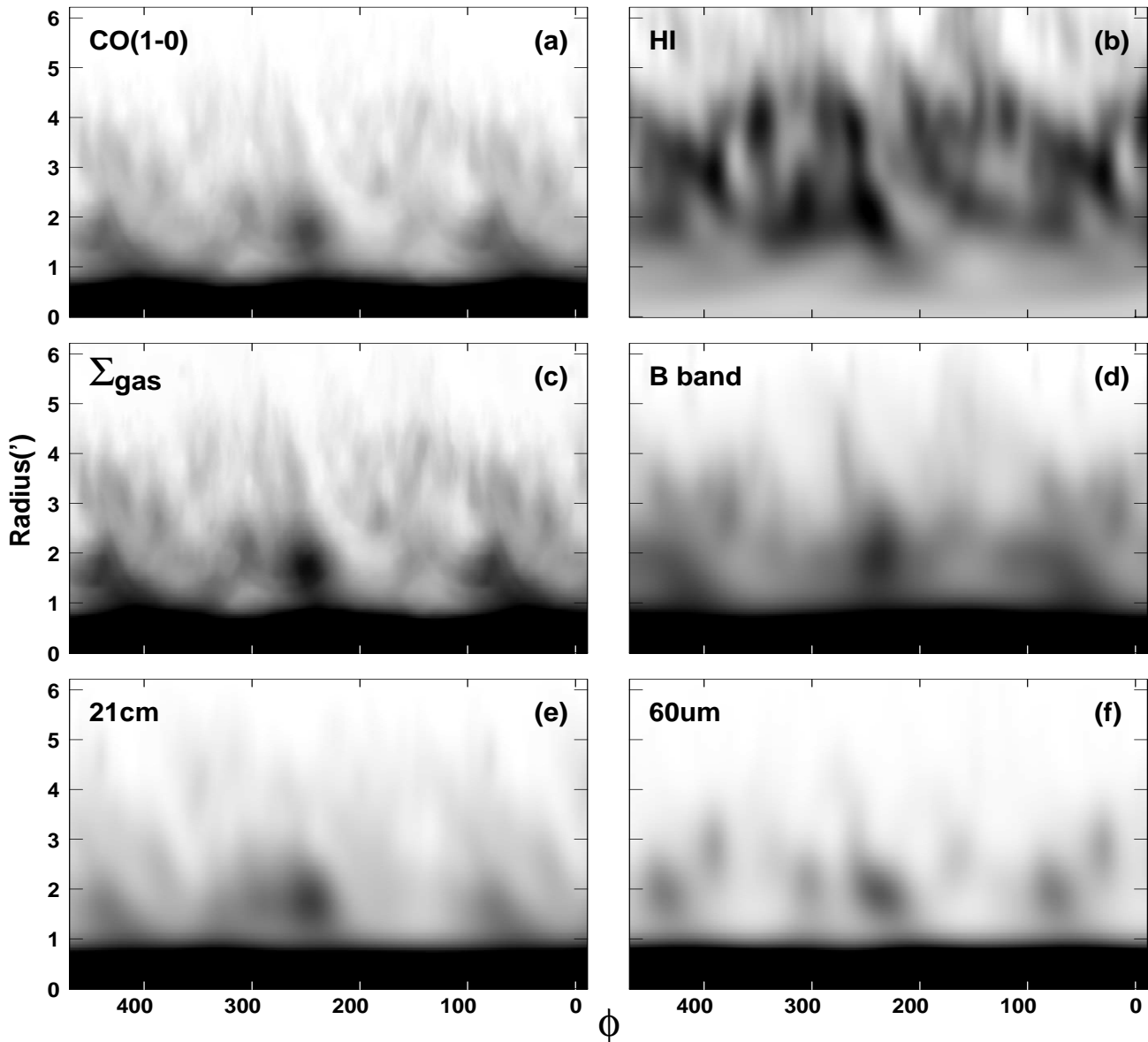


FIG. 12.—Polar maps of the disk of M83. Polar maps of M83 have been corrected to a face-on view of the galaxy. North is located at $\phi = 0^\circ, 360^\circ$, and ϕ runs counterclockwise from north. Rotation of the galaxy is left to right in the maps. The gas, optical, and continuum maps were convolved to $55''$ resolution, matching the CO beam. In each case the gray scale was selected to bring out features in the disk. (a) I_{10} gray scale runs from 0 to 40 K km s^{-1} . (b) I_{HI} gray scale runs from 0 to $2.1 \text{ Jy beam}^{-1} \text{ km s}^{-1}$. (c) Σ_{gas} gray scale runs from 0 to $150 M_\odot \text{ pc}^{-2}$. (d) B-band optical gray scale is uncalibrated. (e) 21 cm continuum gray scale runs from 0 to 60 mJy . (f) $60 \mu\text{m}$ continuum gray scale runs from 25 to 300 MJy sr^{-1} .

at the nucleus ($\sim 11 \text{ km s}^{-1}$), is near 0 km s^{-1} along the kinematic major axis (which is close to the bar major axis), and is at an azimuthal maximum along the kinematic minor axis. Because the rotation component is seen at low inclination and is subtracted in quadrature from the larger observed component, removal of the dispersion component due to galactic rotation in the beam does not significantly change the velocity dispersion patterns shown in Figure 14. The disturbed appearance of the H I isovelocity contours caused by warping is echoed in the $\sigma_{\text{H I}}$ peaks seen in the outer H I disk, another indication that the gas disk has been severely perturbed.

All three [CO (1–0), CO (2–1), H I] of the dispersion maps peak with $\sim 36 \text{ km s}^{-1}$ (rms) at or near the nucleus and fall rapidly outside of the nucleus to mean disk values on the order of $10\text{--}15 \text{ km s}^{-1}$. The similarity in the $\sigma_{\text{H I}}$ and σ_{CO}

over the inner disk implies that the molecular and atomic gas phases are well mixed. This differs from the Galaxy in which the mean $\sigma_{\text{H I}}$ is nearly twice the mean σ_{CO} (Malhotra 1994, 1995).

A Brandt model rotation curve was fitted to the inner disk, cutting off the fit at the point where the warp begins. Parameters for the Brandt model fit are listed in Table 1 and are similar to those of Huchtmeier & Bohnenstengel (1981). The Brandt model rotation curve fits to the CO and H I data are shown in Figure 15. The inner $10'$ disk is neatly fitted by a simple circular rotation model, despite the severe warping so plainly evident for the outer disk. It would appear that the inner disk has resisted distortion by whatever caused the warping of the outer disk.

A velocity residuals pattern, obtained by subtracting the model circular velocities from the observed velocity field,

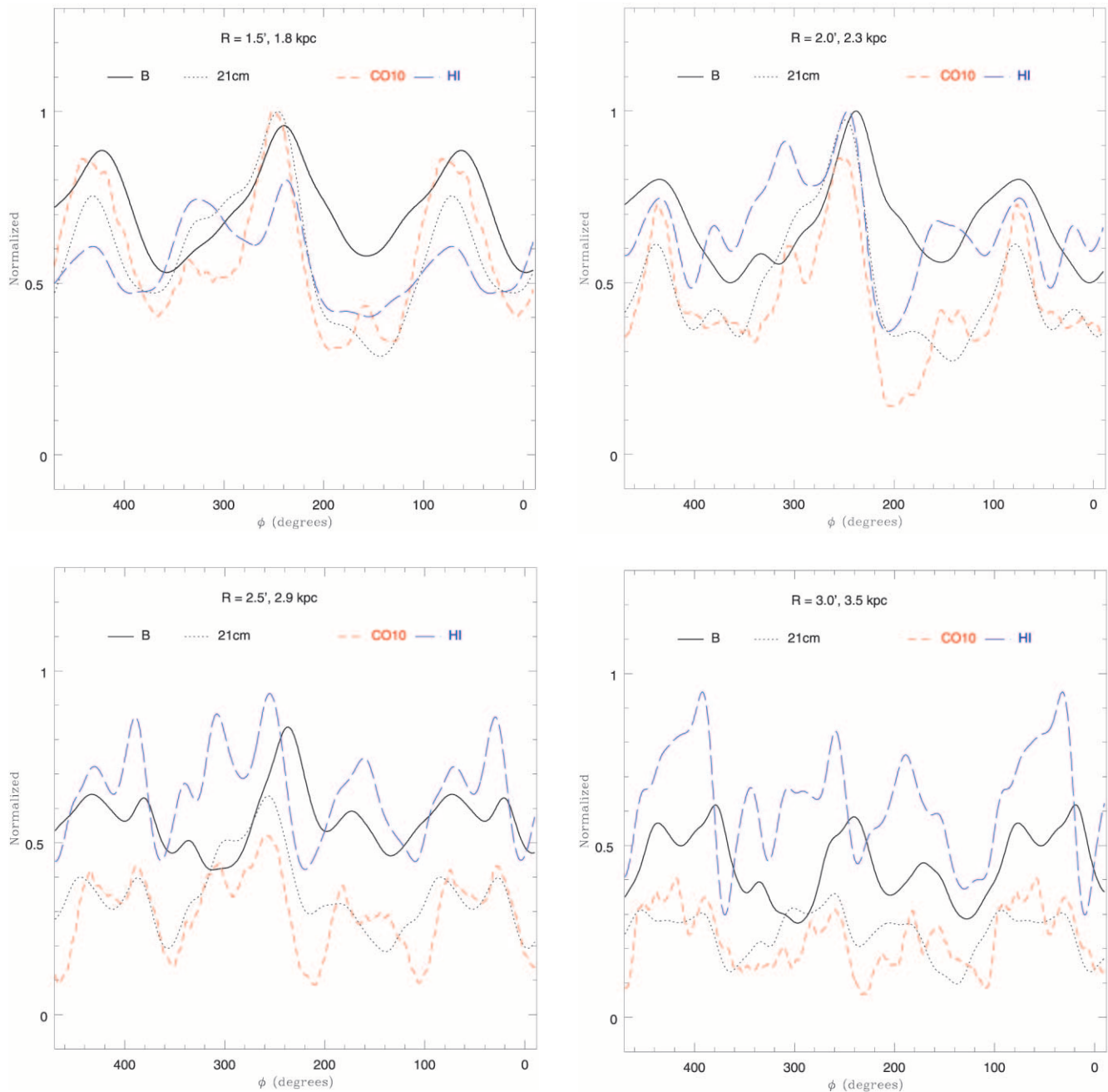


FIG. 13.—Azimuthal slices through polar plots, all at $55''$ resolution, corrected to a face-on view of M83. North is located at $\phi = 0^\circ, 360^\circ$, and ϕ runs counterclockwise from north. Rotation of the galaxy is left to right in the plots. In each case, the emission has been divided by the peak emission found in all the slices, so the various curves are normalized to this peak for each tracer. Slices were taken in increments of $0.5'$ between radii of $1.5' - 5.0'$, beyond which azimuthal coverage in CO is incomplete. On this normalized scale the 1σ emission in the B -band profiles is less than 0.01 and 0.02 for the 21 cm continuum. The single channel 1σ emission for the CO (1–0) profile is 0.01 and 0.02 for H I.

lacks a clear pattern of approaching-receding velocity arm pairs in either the H I or CO data that might allow us to locate the corotation radius using Canzian's method (Canzian 1993; Canzian & Allen 1997). Tilanus & Allen (1993) also failed to find streaming motions across spiral arms in either H β or H I observations of M83.

To summarize, the CO and H I kinematics of the inner $10'$ disk is consistent with an inner gas disk that is dominated by the molecular gas. The same discontinuity in gas phase moving from molecular inner to atomic outer gas disk is seen in

the gas kinematics: rather normal isovelocity contours in the inner $10'$ disk, in sharp contrast to the very disturbed isovelocity contours of the warped outer disk.

6. WHY DOES CO FALL OFF RAPIDLY AT A RADIUS OF $5'$ IN M83?

M83 has a hard edge where CO emission disappears and H I falls off steeply. The gas falloff happens to occur where the nonaxisymmetric velocity disturbance of the warp

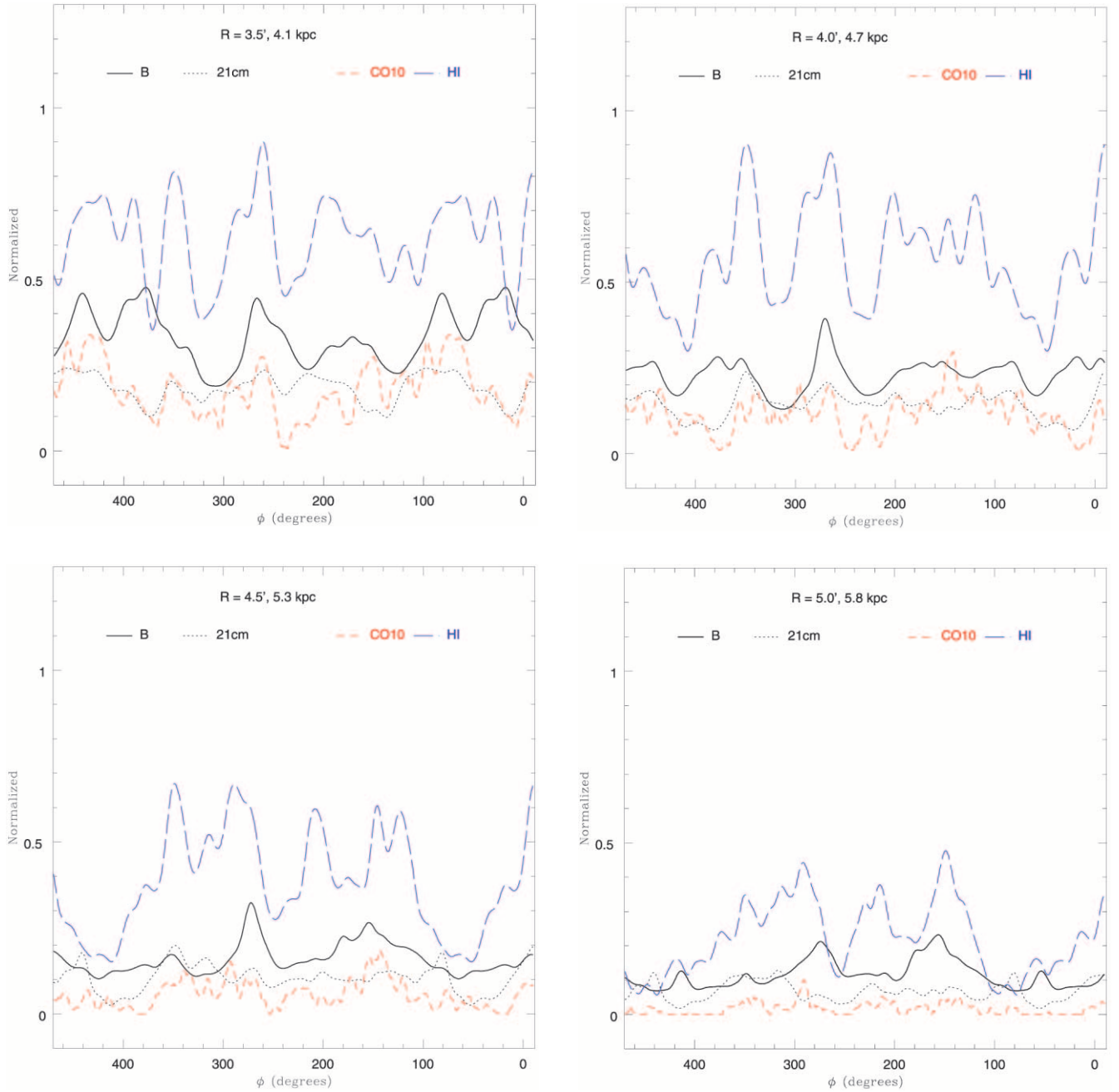


FIG. 13.—Continued

shows up. What causes this hard edge? Is it a property of the gas disk itself that is incidentally related to the warp? Or is it a direct consequence of the warp?

It has been proposed that the ISM pressure, P_{ISM} , plays a large role in determining the relative fraction of a cloud's mass that will be in molecular form (Maloney 1988; Elmegreen 1989), and according to Elmegreen & Parravano (1994), there exists a P_{min} below which cold, dense molecular clouds cannot form. Elmegreen (1989) derived an expression for the macroscopic midplane P_{ISM} from numerical solutions to equations of hydrostatic equilibrium for a combined gas and stellar disk:

$$P_{\text{ISM}} = \frac{\pi}{2} G \Sigma_{\text{gas}} \left(\Sigma_{\text{gas}} + \Sigma_{\text{stars}} \frac{\sigma_{\text{gas}}}{\sigma_{\text{stars}}} \right),$$

where σ_{gas} and σ_{stars} are the velocity dispersions of the gas and stars, respectively. Without an accurate assessment of the stellar contribution, we can only estimate the magnitude of change in P_{ISM} at the edge of the CO disk. The gas surface density falls by a factor of 10 from 4.5' to 5.5', a span of 1 kpc, while the optical flux (which we presume roughly traces the stellar mass) falls by a factor of 2. For the Galaxy and IC 342, $\sigma_{\text{gas}} < \sigma_{\text{stars}}$, limiting the contribution of the Σ_{stars} term (Malhotra 1994, 1995; Crosthwaite et al. 2001). Therefore, P_{ISM} can be expected to fall by a factor of 20 (if stars dominate the surface density) to 100 (if gas dominates; less likely) over the same span, depending on the magnitude of the stellar contribution. It is possible that a P_{min} threshold is crossed in this range of P_{ISM} , leading to the sudden disappearance of molecular gas, and therefore CO, because of the

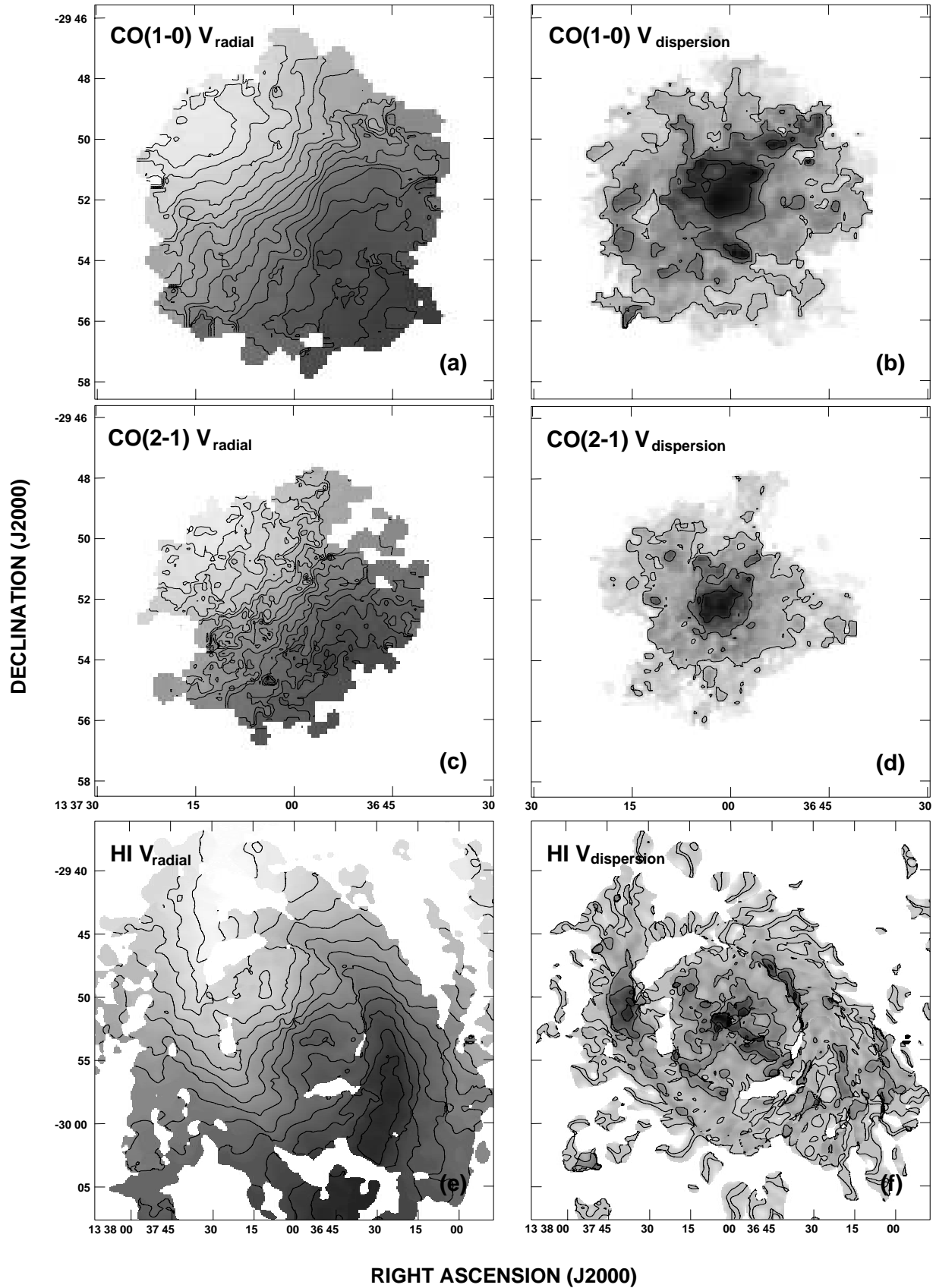


FIG. 14.—M83 CO and H I velocity and velocity dispersion maps. (a) and (b) CO (1–0); (c) and (d) CO (2–1); (e) and (f) H I. For the CO maps the intensity-weighted velocity maps are contoured at 10 km s^{-1} spacings for $420\text{--}590 \text{ km s}^{-1}$. For the CO dispersion maps contours are at 10, 20, and 30 km s^{-1} , with a peak velocity dispersion of 36 km s^{-1} . For the H I map the intensity-weighted velocity maps are contoured at 20 km s^{-1} spacings for $400\text{--}640 \text{ km s}^{-1}$. For the H I dispersion map contours are at 10, 15, 20, and 25 km s^{-1} , with a peak velocity dispersion of 35 km s^{-1} .

TABLE 1
GLOBAL PROPERTIES OF M83

Property	Value
Hubble type ^a	Sbc
R.A. (J2000.0) ^b	13 37 00.8
Dec. (J2000.0) ^b	-29 51 58
Distance ^c (Mpc).....	4
v_{LSR}^d (km s ⁻¹).....	516
Inclination ^d (deg).....	25
Position angle ^d (deg).....	226
V_{max}^d (km s ⁻¹).....	170
$R_{V_{\text{max}}}^d$ (arcmin).....	4.2 (7.3 kpc)
n^d	1.5
$M_{\text{H}_2}^e$ (M_{\odot}).....	2.5×10^9
$M_{\text{H I}}$ (VLA map $R < 5'$) (M_{\odot}).....	5.1×10^8
$M_{\text{H I}}$ (total) ^f (M_{\odot}).....	6.2×10^9
M_{dyn}^g (M_{\odot}).....	7.0×10^{10}

NOTE.—Units of right ascension are hours, minutes, and seconds, and units of declination are degrees, arcminutes, and arcseconds.

^a Obtained from the NASA/IPAC Extragalactic Database.

^b Dynamical center based on fit of Brandt rotation model.

^c de Vaucouleurs 1979.

^d Kinematic parameters from fit of Brandt rotation model.

^e Using the standard conversion factor, 2×10^{20} K km s⁻¹.

^f Huchtmeier & Bohnenstengel 1981, adjusted to 4 Mpc distance.

^g Total dynamical mass based on Brandt model fit parameters.

falloff in total (H I + H₂) gas surface density. This is quite different from the spiral galaxy IC 342, where P_{ISM} appears to fall off gradually over the 5 kpc radial range of the CO disk (Crosthwaite et al. 2001) and a stellar disk that appears

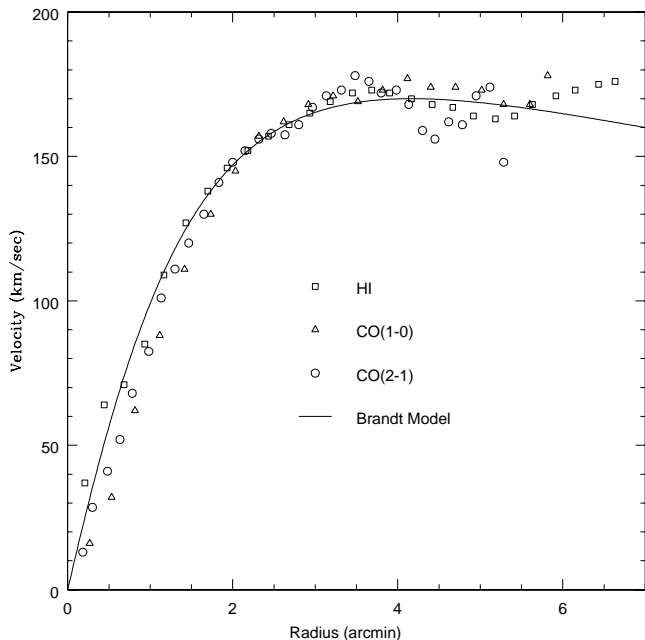


FIG. 15.—Rotation curve for the inner disk of M83. CO and H I circular velocities are plotted along with the adopted Brandt model rotation curve originally fitted to H I 21 cm line observations of M83.

to diminish slowly at radii greater than 7 kpc (Buta & McCall 1999). There are locations in the outer H I disk, $R \sim 9'$ (10 kpc), where the Σ_{gas} has the same magnitude as the gas at the edge of the CO disk. In these locations the partial pressure of the gas may be sufficient to promote the formation of CO.

There is a distinct discontinuity in the H I radial velocity field at the edge of the CO disk, the beginning of the warped outer gas disk (Fig. 14e). This discontinuity could be accompanied by a kinematic shear capable of destroying marginally bound H₂ clouds that would be bound in an otherwise unperturbed disk. The disruption of the molecular clouds could leave them open to photodissociation from the interstellar radiation field. This converted gas should show up as H I, producing a smooth transition in the total gas surface density. However, this is not seen. Instead we see local minimum unlike the monotonically decreasing gas surface density seen in other spiral galaxies, like IC 342 (Crosthwaite et al. 2001).

In summary, the sharp decline in CO emission at the beginning of the warp appears to be related to the decline in total gas surface density since they occur at the same location. A P_{min} threshold for the formation of molecular clouds may be crossed at this radius in M83.

7. CO EXCITATION IN M83: DENSITIES AND TEMPERATURES IN THE MOLECULAR GAS

A map of the ratio of the integrated intensities of the CO (2–1) and CO (1–0) lines, $r_{12} = I_{21}/I_{10}$, is presented in Figure 16a. The ratio map was produced from greater than 3σ data after convolving the CO (2–1) channel cube to the beam size of the CO (1–0) data. We estimate that the uncertainties in r_{12} are on the order of 20%.

The bar and arm pattern is loosely traced by the $r_{12} = 1.2$ contour. At the nucleus, along the bar and much of the strong arm pattern r_{12} is 1. In the disk, outside of the bar, r_{12} spans a wide range, from the minimum, 0.4, to values greater than 2. The mean r_{12} for the disk is 1.1 ± 0.2 , significantly higher than the 0.66 mean value for the Galactic disk (Sakamoto et al. 1995, 1997). Wiklind et al. (1990) also found high r_{12} values in M83.

In principle, r_{12} gives information on the excitation of the CO emission, T_{ex} , and the kinetic temperature, T_k . The observed main-beam temperature at frequency ν is related to a Planck function, $B_\nu(T_{\text{ex}})$, by the areal beam filling factor, f_a , and radiative transfer through an optical depth, τ_ν :

$$T_{\text{mb}} = f_a \frac{c^2}{2k\nu^2} [B_\nu(T_{\text{ex}}) - B_\nu(T_{\text{CMB}})] (1 - e^{-\tau_\nu}),$$

which includes a correction for the cosmic microwave background contribution to the beam, $B_\nu(T_{\text{CMB}})$, at 2.73 K. If we assume that f_a is the same for both lines, both lines are optically thick ($\tau_\nu \gg 1$), and the emission can be characterized by a single T_{ex} , we can naively derive T_{ex} values for the emission: $r_{12} = 0.8$ corresponds to $T_{\text{ex}} = 10$ K, while $r_{12} = 0.5$ corresponds to $T_{\text{ex}} = 3.5$ K (r_{12} is not unity because of the Rayleigh-Jeans correction for intensity). Higher values of the ratio are typically found in the nuclear regions of starburst galaxies where elevated star formation heats the molecular gas, while values lower than 0.8 are typical of cold or subthermally excited ($T_{\text{ex}} < T_k$) disk molecular clouds. Values of $r_{12} > 0.8$ indicate optically thin gas

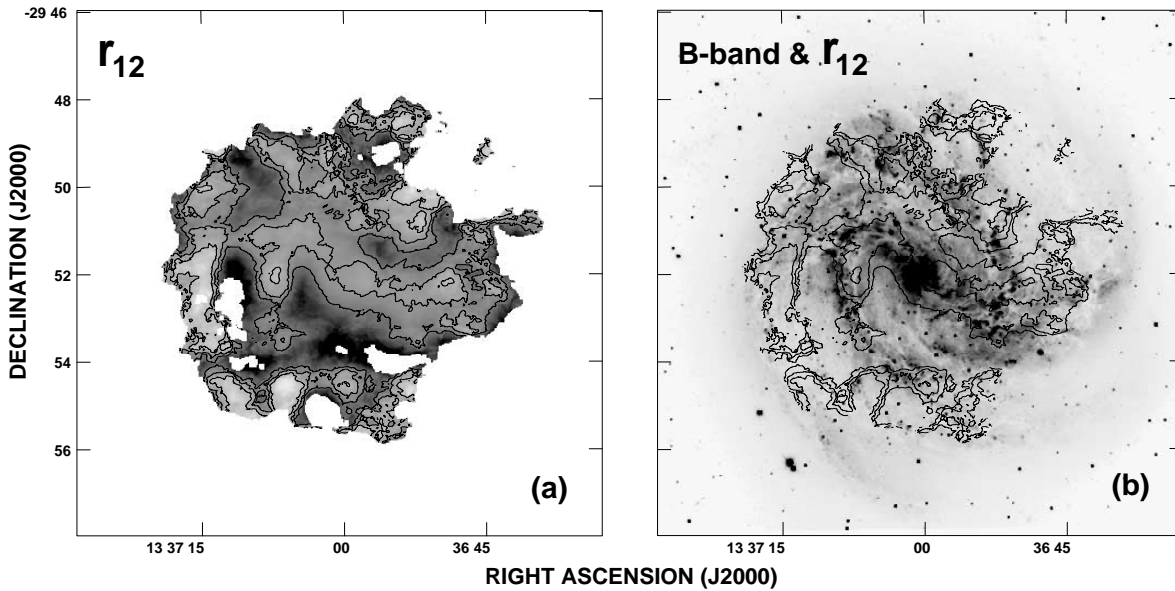


FIG. 16.—CO (2–1)/CO (1–0) ratio in M83. (a) $r_{12} = I_{21}/I_{10}$. The gray scale ranges from 0 (*light*) to 2 (*dark*). Contours are at 0.8, 1.0, and 1.2. (b) *B*-band optical image (provided by R. Tilanus) with r_{12} contours of (a).

unless $T_{\text{ex}} > 10$ K, unlikely outside of the nucleus on these size scales.

At the bright CO nucleus, $r_{12} \sim 1.0 \pm 0.1$. Wiklind et al. (1990) found nuclear ratios of ~ 1 with marginally higher resolution Swedish-ESO Submillimetre Telescope (SEST) observations. These ratios could imply $T_{\text{ex}} > 20$ K, optically thick, molecular gas as suggested by Aalto (1994). $T_{\text{ex}} > 20$ K is reasonable for the nuclear region that has a starburst. Petipnas & Wilson (1998) interpret the changes in morphology between $\sim 15''$ resolution observations (JCMT) of CO (4–3) and CO (3–2) and other published high-resolution maps of CO (1–0) in the nucleus of M83 as resulting from the depopulation of low- J states in hot gas.

Along the bar and arm regions (Fig. 16*b*), r_{12} is also 1.0 ± 0.2 . Wiklind et al. (1990) found ratios of ~ 1 in the limited arm region contained in their SEST map. The implied $T_{\text{ex}} > 20$ K for optically thick emission is much higher than expected for regions outside of the nucleus. For comparison, in the Milky Way arms $r_{12} \sim 0.73$ (Sakamoto et al. 1995, 1997) with an implied $T_{\text{ex}} \sim 7$ K, in agreement with observed brightness temperatures (Scoville et al. 1987). A value of 0.8, consistent with $T_{\text{ex}} \sim 10$ K and similar to the Milky Way, is just consistent with our observations.

Possibly the most peculiar aspect of the ratio maps is the wide range of r_{12} values found outside of the bar/arm pattern (Fig. 16*b*). By comparison to Galactic interarm gas, we expect to see $r_{12} \sim 0.5$ – 0.7 , which corresponds to T_{ex} in the 4–7 K range for thermalized emission, and/or regions where $r_{12} < 0.6$, indicating cold or subthermally excited molecular emission (Sakamoto et al. 1997). Low values are indeed seen in the outer disk of M83 particularly to the northwest and southeast with some of the ratios as low as 0.5, which could indicate 3.5 K molecular gas. However, a large fraction of the interarm disk has $r_{12} > 0.8$. The standard interpretation, based on optically thick thermalized CO, would indicate much warmer ($T_{\text{ex}} > 10$ K) molecular gas than would normally be expected in interarm gas of the outer disk. In addition, there are several interarm regions where $r_{12} > 1.2$. High ratios, ~ 1.8 , for interarm gas were also found by

Wiklind et al. (1990) in the region southeast of the nucleus. In our r_{12} map, high- and low-ratio regions are juxtaposed. An experiment, using only greater than 4σ CO data, resulted in a reduced radius for the ratio map, but the high/low- r_{12} regions remained; the unusual ratios are not merely a consequence of using low signal-to-noise ratio data.

Why do we see high ratios for molecular gas outside of the nucleus? In particular, why are there widespread interarm regions with $r_{12} > 1$? We consider four possible explanations and their caveats:

1. The simplest interpretation is that the high-ratio CO emission is optically thin. The high- r_{12} regions do tend to lie along areas of low column density, and the anticorrelation of r_{12} and N_{H_2} is suggestive. For optically thin CO with $r_{12} \sim 1.3 \pm 0.5$, $T_{\text{ex}} \sim 7.5 \pm 2.5$ K. The mean I_{10} in these regions is 5.4 ± 0.6 K km s $^{-1}$, which corresponds to $N_{\text{H}_2} \sim (3 \pm 1) \times 10^{19}$ cm $^{-2}$ for optically thin gas, a factor of 40 down from values obtained using the standard conversion factor. Once the contribution to the total hydrogen column density from H I is added to the optically thin N_{H_2} , the mean visual extinction through the neutral gas column is found to be $\langle A_v \rangle \sim 0.4 \pm 0.2$ mag (Frerking, Langer, & Wilson 1982). Because CO is self-shielding, for $A_v < 0.5$ and near-solar metallicities there is little CO (Tielens & Hollenbach 1985; Hollenbach, Takahashi, & Tielens 1991), implying that the filling factor of this gas is $\sim 50\%$. Optically thin, kiloparsec-scale CO emission has not been detected in the Galaxy, leading us to question whether this is what is actually happening in M83. Wiklind et al. (1990) proposed a two-component model that preserves the use of CO (1–0) emission as a molecular mass tracer with X_{CO} . Their solution suggests that 60% of the emission comes from overly emissive, optically thin gas with $T_{\text{ex}} \sim 40$ K and a filling factor of 0.8. The remainder comes from underemissive, optically thick and small gas clouds that account for 90% of molecular mass. This solution still requires kiloparsec-scale, optically thin CO and, in addition, requires unusually warm disk CO.

2. The high-ratio region contains thermalized CO (2–1) but subthermal CO (1–0). Large velocity gradient (LVG) modeling has shown that there is a narrow range of densities, $n_{\text{H}_2} \sim 5000 \text{ cm}^{-3}$, and kinetic temperatures, $T_k \sim 80 \text{ K}$, which will produce r_{12} slightly larger than unity (Sakamoto 1993). The range of physical conditions is too narrow and too extreme to be realistic for kiloparsec-scale CO.

3. The $r_{12} \sim 1$ are due to temperature gradients (caused by strong, external, UV radiation fields from OB stars) in the CO-emitting photospheres of molecular clouds (Gierens, Stutzki, & Winnewisser 1992; Köster et al. 1994; Störzer et al. 2000). The CO (2–1) emission becomes optically thick closer to the photodissociation region surface than the CO (1–0) emission, and the two lines end up having different characteristic T_{ex} , leading to the higher r_{12} . High ratio values found for Milky Way molecular gas have been attributed to this type of external heating (Castets et al. 1990; Oka et al. 1996, 1998; Sakamoto et al. 1997). It seems to be operating on $\sim 100 \text{ pc}$ size scales in the massive clouds found in the nucleus of IC 342 (Turner, Hurt, & Hudson 1993; Meier, Turner, & Hurt 2000) and could operate in the nucleus of M83 as well. However, the Galactic molecular gas associated with $r_{12} \sim 1$ is localized to regions of massive star formation and does not strongly affect r_{12} on kiloparsec scales.

4. The high r_{12} are due to temperature gradients caused by strong external radiation fields from non-OB stars (Spaans et al. 1994). While the radiation field from 6000 K stars contains far fewer UV photons than that of OB stars, the efficiency of photoelectric grain heating per UV photon is higher because the grains are more electrically neutral in the relative absence of UV radiation. Again, the two CO lines end up with different characteristic T_{ex} , leading to $r_{12} > 1$, but this time without massive stars. The model still requires a high incident radiation field, 10^3 times the solar neighborhood value.

None of these explanations are completely satisfactory when compared with what we know about Galactic H_2 . The optically thin solutions carry with them the possibility that the standard conversion factor based on a Galactic calibration may not be applicable to M83. We may be seeing highly emissive, optically thin gas filling a large fraction of the beam, resulting in a high r_{12} , while optically thick, potentially very cold CO that should trace molecular mass remains undetected or undercontributes to the observed emission.

8. CONCLUSIONS

We have presented fully sampled images of CO (1–0) and CO (2–1) emission in the spiral galaxy M83, with the following findings:

1. The CO (1–0) and CO (2–1) emission shows many of the same features seen in the optical disk, a strong nuclear peak of emission, a prominent bar, and molecular gas arms, all within a $10'$ diameter inner disk filled with CO emission.

We obtain $M_{\text{H}_2} = 2.5 \times 10^9 M_{\odot}$ for the molecular mass of M83.

2. Molecular gas dominates the total gas surface density in the inner $10'$ diameter of M83, where $\sim 80\%$ of the total gas mass is H_2 . Molecular gas more than fills the central depression in the H I disk. Averaged over the remainder of the CO disk, the molecular surface density is $\Sigma_{\text{H}_2} = 20 M_{\odot} \text{ pc}^{-2} \sim 5\Sigma_{\text{H I}}$.

3. We find an excellent spatial correlation between CO (1–0) emission (or total gas surface density) and 21 cm continuum; the ratios are relatively flat over much of the disk of M83.

4. We see a good spatial and radial correlation between CO (1–0) and $100 \mu\text{m}$ emission, although the $100 \mu\text{m}$ bar is offset from the CO bar. Good spatial correlations are also seen between CO (2–1) emission and $60 \mu\text{m}$ emission, which appear to trace warmer molecular gas and dust than CO (1–0) and $100 \mu\text{m}$. The decline in the ratio of CO to FIR inside of 1.5 may be due to a higher star formation efficiency relative to the amount of molecular gas in the vicinity of the starburst nucleus.

5. Polar plots reveal a complex pattern of offsets between maxima and minima in the azimuthal distribution of CO, H I, 21 cm continuum, and optical emission, as well as a complex pattern of bifurcating spiral arms. Interarm CO is clearly seen in these plots.

6. Kinematically the H I and CO disks are very similar over the region of overlap. The region of the disk containing CO appears to be kinematically distinct from the outer, strongly warped, disturbed outer H I disk. Elevated velocity dispersions are seen along the bar but also perpendicular to the bar along the minor axis of M83's inclined disk.

7. The CO disk of M83 has a hard edge. The edge is coincident with a steep decline in H I emission and the start of strong kinematic warping of the outer disk. If a minimum ISM pressure for the formation of molecular gas exists, that boundary may be crossed at this location.

8. The mean value for r_{12} in the disk of M83 is ~ 1.1 , high by Galactic standards. Over the nucleus and the bar $r_{12} \sim 1$. Over the remainder of the CO disk r_{12} varies between 0.4 and greater than 2 with the largest variation in the interarm regions. Possible interpretations are as follows: the high r_{12} at the nucleus represents $T_{\text{ex}} \geq 20 \text{ K}$, optically thick CO; the low r_{12} in the outer disk represents $T_{\text{ex}} < 7 \text{ K}$ CO; or the high r_{12} in the interarm regions probably represents optically thin CO.

We would like to thank the NRAO 12 m telescope operators, Duane Clark, Paul Hart, Victor Gasho, and Harry Stahl, for their help and company during the many observing sessions in which the data for M83 were acquired. We wish to thank J. van der Hulst for giving us permission to retrieve the H I 21 cm line observations from the VLA archive, and we wish to thank R. Tilanus for providing us with the optical image. This work was supported in part by NSF grant AST 00-71276. We made use of the NASA/IPAC/IRAS HiRes data reduction facilities.

REFERENCES

- Aalto, E. S. 1994, Ph.D. thesis, Chalmers Univ. of Technology
 Adler, D. S., Allen, R. J., & Lo, K. Y. 1991, *ApJ*, 382, 475
 Allen, R. J. 1992, *ApJ*, 399, 573
 Arimoto, N., Sofue, Y., & Tsujimoto, T. 1996, *PASJ*, 48, 275
 Bica, M. D., & Helou, G. 1990, *ApJ*, 362, 59
 Bica, M. D., Helou, G., & Condon, J. J. 1989, *ApJ*, 338, L53
 Bohlin, R. C., Cornett, R. H., Hill, J. K. Smith, A. M., & Stecher, T. P. 1983, *ApJ*, 274, L53
 Buta, R. J., & McCall, M. L. 1999, *ApJS*, 124, 33
 Canzain, B. 1993, *ApJ*, 414, 487

- Canzain, B., & Allen, R. J. 1997, *ApJ*, 479, 723
- Castets, A., et al. 1990, *A&A*, 234, 469
- Christodoulou, D. M., Tohline, J. E., & Steiman-Cameron, T. Y. 1993, *ApJ*, 416, 74
- Clemens, D. P., Sanders, D. B., & Scoville, N. Z. 1988, *ApJ*, 327, 139
- Combes, F. 1991, *ARA&A*, 29, 195
- Combes, F., Encrenaz, P. J., Lucas, R., & Weliachew, L. 1978, *A&A*, 67, L13
- Crosthwaite, L. P., Turner, J. L., Hurt, R. L., Levine, D. A., Martin, R. F., & Ho, P. T. P. 2001, *AJ*, 122, 797
- Dahmen, G., Huttemeister, S., Wilson, T. L., & Mauersberger, R. 1998, *A&A*, 331, 959
- Deutsch, E. W., & Allen, R. J. 1993, *AJ*, 106, 1812
- de Vaucouleurs, G. 1979, *AJ*, 84, 1270
- de Vaucouleurs, G., de Vaucouleurs, A., & Corwin, H. 1976, *Second Reference Catalogue of Bright Galaxies* (Austin: Univ. Texas Press)
- Elmegreen, B. G. 1989, *ApJ*, 338, 178
- Elmegreen, B. G., & Parravano, A. 1994, *ApJ*, 435, L121
- Frerking, M. A., Langer, W. D., & Wilson, R. W. 1982, *ApJ*, 262, 590
- Gierens, K. M., Stutzki, J., & Winnewisser, G. 1992, *A&A*, 259, 271
- Handa, T., Nakai, N., Sofue, Y., Hayashi, M., & Fujimoto, M. 1990, *PASJ*, 42, 1
- Helou, G., & Bicay, M. D. 1993, *ApJ*, 415, 93
- Hollenbach, D. J., Takahashi, T., & Tielens, A. G. G. M. 1991, *ApJ*, 377, 192
- Huchtmeier, W. K., & Bohnenstengel, H. D. 1981, *A&A*, 100, 72
- Hunter, S. D., et al. 1997, *ApJ*, 481, 205
- Kenney, J. D. P., & Lord, S. D. 1991, *ApJ*, 381, 118
- Köster, B., Störzer, H., Stutzki, J., & Sternberg, A. 1994, *A&A*, 284, 545
- Kulkarni, S. R., & Heiles, C. 1987, in *Interstellar Processes*, ed. D. J. Hollenbach & H. A. Thronson (Dordrecht: Reidel), 87
- Kutner, M. L., & Ulich, B. L. 1981, *ApJ*, 250, 341
- Lord, S. D., & Kenney, J. D. P. 1991, *ApJ*, 381, 130
- Malhotra, S. 1994, *ApJ*, 433, 687
- . 1995, *ApJ*, 448, 138
- Maloney, P. 1988, *ApJ*, 334, 761
- Mangum, J. G. 1996a, *On the Fly Observing at the 12 m (Socorro: NRAO 12 m Publ.)*
- . 1996b, *User's Manual for the NRAO 12 m Millimeter-Wave Telescope (Socorro: NRAO 12 m Publ.)*
- . 1997, *Equipment and Calibration Status for the NRAO 12 m Telescope (Socorro: NRAO 12 m Publ.)*
- Meier, D. S., & Turner, J. L. 2001, *ApJ*, 551, 687
- Meier, D. S., Turner, J. L., & Hurt, R. L. 2000, *ApJ*, 531, 200
- Oka, T., Hasegawa, T., Handa, T., Hayashi, M., & Sakamoto, S. 1996, *ApJ*, 460, 334
- Oka, T., Hasegawa, T., Hayashi, M., Handa, T., & Sakamoto, S. 1998, *ApJ*, 493, 730
- Petitpas, G. R., & Wilson, C. D. 1998, *ApJ*, 503, 219
- Rand, R. J., Lord, S. D., & Higdun, J. L. 1999, *ApJ*, 513, 720
- Rieke, G. H. 1976, *ApJ*, 206, L15
- Rogstad, D. H., Lockhart, I. A., & Wright, M. C. H. 1974, *ApJ*, 193, 309
- Rots, A. H. 1979, *A&A*, 80, 255
- Rumstay, K. S., & Kaufman, M. 1983, *ApJ*, 274, 611
- Sage, L. J. 1993, *A&A*, 272, 123
- Sage, L. J., Salzer, J. J., Loose, H. H., & Henkel, C. 1992, *A&A*, 265, 19
- Sage, L. J., & Solomon, P. M. 1989, *ApJ*, 342, L15
- Sakamoto, S. 1993, Ph.D. thesis, Univ. Tokyo
- Sakamoto, S., Hasegawa, T., Handa, T., Hayashi, M., & Oka, T. 1997, *ApJ*, 486, 276
- Sakamoto, S., Hasegawa, T., Hayashi, M., Handa, T., & Oka, T. 1995, *ApJS*, 100, 125
- Scoville, N. Z., & Sanders, D. B. 1987, in *Interstellar Processes*, ed. D. J. Hollenbach & H. A. Thronson, (Dordrecht: Reidel) 21
- Scoville, N. Z., Yun, M. S., Clemens, D. P., Sanders, D. B., & Waller, W. H. 1987, *ApJS*, 63, 821
- Sodroski, T. J., et al. 1994, *ApJ*, 428, 638
- Solomon, P. M., Rivolo, A. R., Barrett, J., & Yahil, A. 1987, *ApJ*, 319, 730
- Spaans, M., Tielens, A. G. G. M., van Dishoeck, E. F., & Bakes, E. L. O. 1994, *ApJ*, 437, 270
- Sparke, L. S. 1984a, *ApJ*, 280, 117
- . 1984b, *MNRAS*, 211, 911
- Sparke, L. S., & Casertano, S. 1988, *MNRAS*, 234, 873
- Störzer, H., Zielinsky, M., Stutzki, J., & Sternberg, A. 2000, *A&A*, 358, 682
- Strong, A. W., et al. 1988, *A&A*, 207, 1
- Suchkow, A., Allen, R. J., & Heckman, T. M. 1993, *ApJ*, 413, 542
- Telesco, C. M., Wolstencroft, R. D., & Done, C. 1988, *ApJ*, 329, 174
- Tielens, A. G. G. M., & Hollenbach, D. 1985, *ApJ*, 291, 722
- Tilanus, R. P. J., & Allen, R. J. 1993, *A&A*, 274, 707
- Trinchieri, G., Fabbiano, G., & Paulumbo, G. G. C. 1985, *ApJ*, 290, 96
- Turner, J. L., & Ho, P. T. P. 1994, *ApJ*, 421, 122
- Turner, J. L., Ho, P. T. P., & Beck, S. C. 1987, *ApJ*, 313, 644
- Turner, J. L., Hurt, R. L., & Hudson, D. Y. 1993, *ApJ*, 413, L19
- Ulich, B. L., & Hass, R. W. 1976, *ApJS*, 30, 247
- Verter, F., & Hodge, P. 1995, *ApJ*, 446, 616
- Wiklind, T., Rydbeck, G., Hjalmarson, A., & Bergman, P. 1990, *A&A*, 232, L11
- Wilson, C. D. 1995, *ApJ*, 448, L97
- Young, J. S., et al. 1995, *ApJS*, 98, 219
- Young, J. S., & Knezek, P. M. 1989, *ApJ*, 347, L55
- Young, J. S., & Scoville, N. Z. 1982, *ApJ*, 258, 467
- . 1991, *ARA&A*, 29, 581